

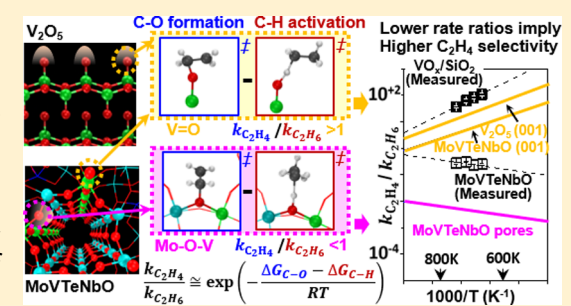
Effects of Lattice O Atom Coordination and Pore Confinement on Selectivity Limitations for Ethane Oxidative Dehydrogenation Catalyzed by Vanadium-Oxo Species

Yilang Liu, Leelavathi Annamalai, and Prashant Deshlahra*

Department of Chemical and Biological Engineering, Tufts University, Medford, Massachusetts 02155, United States

Supporting Information

ABSTRACT: M1-phase MoVTeNb mixed oxides contain V-oxo species isolated by dispersion in the Mo-oxo framework and onedimensional heptagonal micropores that tightly enclose C₂H₆ molecules. These oxides catalyze C_2H_6 oxidation with C_2H_4 selectivity much higher than V₂O₅ oxides containing continuous V-oxo domains without micropores. Here, effects of the structures of VO_x domains and of the micropores on the selectivity are discerned using (i) measured rate constant ratios and activation barrier differences relevant to selectivity on the two oxides and (ii) density functional theory (DFT) analysis of steps mediating C-H activation in C2H6 and C2H5 radicals and unselective C-O bond formations in C₂H₅ radicals and C₂H₄ molecules



on (001) surfaces of both oxides and in pores of MoVTeNb oxides. The DFT-derived values of kinetic parameters representing C₂H₄ selectivities and activation energy differences between C₂H₄ formation and C-O bond formation steps on V₂O₅(001) are similar to measured values. In contrast, for MoVTeNb oxides, the DFT-derived selectivity inside the pores is much higher than measurements, while that on the (001) surfaces is much lower, suggesting that measured selectivity represents contributions from C-H activations inside the pores and unselective steps inside pores as well as on (001) surfaces. The selectivity on (001) surfaces is similar in V₂O₅ and MoVTeNb oxides, indicating that the isolation of V-oxo domains within this surface leads to only small changes in selectivity, while the pores lead to much higher selectivity. The descriptors of the selectivity trends on such transition metal oxide surfaces are derived by examining C₂H₄ epoxidation and C₂H₆ C-H activation transition-state energies and molecule-surface van der Waals (vdW) interactions and steric forces that influence these energies on a variety of O atoms with different electronic and structural properties on (001) surfaces and inside the pores. High C₂H₄ selectivity requires that the O atoms in oxides exhibit lower tendency to form C-O bonds in C_2H_4 than to activate C-H bonds in C_2H_6 , which depends strongly on the H atom addition energies of oxides and O atom coordination. V₂-O-V tri-coordinated and V-O-V or V-O-Mo bridging O atoms require significantly greater energy penalty than V=O terminal O atoms for the metal-oxygen framework distortions required for forming C-O bonds; these distortion energies reflect steric hindrance to forming C-O bonds, which leads to higher epoxidation transition-state energy and indicates higher C₂H₄ selectivity in tri-coordinated and bridging O atoms. The high selectivity inside the heptagonal pores originates from the inaccessibility to terminal O atoms in addition to much stronger vdW interactions and more significant steric distortion energies in tight pores. These analyses suggest that H atom addition energies, vdW interaction energies, and catalyst distortion energies are relevant descriptors of selectivity for both intrapore and external O atoms.

1. INTRODUCTION

Metal oxides containing vanadium atoms are among the most important catalysts for oxidative dehydrogenation (ODH) of light alkanes.1 These oxides have been prepared and studied in diverse forms with vanadium-oxo species dispersed on nonreducible or reducible oxides, 2-5 are present as cations formed by replacing protons in aluminosilicates⁶⁻⁸ or incorporated within the ordered framework of crystalline oxides, 9-14 and exhibit varying structural, electronic, and catalytic properties. Many vanadium-containing oxides show significant selectivity to C₂H₄ in C₂H₆ oxidative conversions. The selectivity at a given conversion typically increases with increasing reaction temperature, which leads to greater than 50% single pass yields in some oxides but only at high

temperatures typically above 973 K.15 In contrast to other vanadium-containing oxides, MoVTeNb and MoV mixed metal oxides with an M1 crystal phase exhibit high selectivity and yield to C₂H₄ even at temperatures below 673 K,9 indicating that these crystals exhibit properties that are distinct from those achieved by changing compositions in other vanadium-containing catalysts.

C₂H₆ ODH requires two C-H bond activations, but the selectivity to C₂H₄ is limited by the formation of oxygenates, CO and CO₂, either directly from C₂H₆ or via sequential

Received: August 14, 2019 Revised: October 8, 2019 Published: November 8, 2019 reactions of C₂H₄. ¹⁶ The oxygenated products require at least one critical C-O bond formation step that may occur with or without concomitant C-H activations. These oxidative conversions are mediated by Mars-van Krevelen redox cycles with kinetically coupled steps involving reduction of the oxide catalyst by H atom addition or O atom removal at surface oxo species and reoxidation of reduced sites by O₂. 17 Isotopic scrambling measurements suggest that the first C-H bond activation in C₂H₆ on vanadium oxides and the O-O bond activation in reoxidation of reduced sites are irreversible. 18 The reoxidation steps, however, are rapid and kinetically irrelevant, as indicated by reaction rates independent of oxygen pressure, 18,19 which makes C-H activation the rate-limiting step. As a result, oxides that exhibit more negative energy for addition of an H atom to lattice O atoms are more reactive for ODH.^{20,21}

The catalytic properties that influence C_2H_4 selectivity are less well resolved than those describing ODH rates. Acidbase strengths of oxides, involvement of terminal and bridging oxygens, or isolation of active sites has been proposed to influence selectivity but often without significant molecular-level analysis of relevant elementary steps. A wide range of vanadium-containing oxides has been used to probe C–H activation steps using density functional theory (DFT). The parallel and sequential oxidation steps leading to oxygenated products, however, were probed mainly in only a few types of supported VO_x monomers in SiO_x clusters and in a periodic V₂O₅(001) surface. $^{31-35}$

The M1-phase oxides consist of crystals that contain onedimensional pores originating from stacking of layers with rings of five, six, or seven metal atoms (typically Mo or V). 30,36 The diameter of seven-membered ring pores is similar to the molecular size of C₂H₆.³⁷ Studies on these materials tend to propose involvement of either VO_x or TeO_x species on the surfaces of crystals in the most active sites and emphasize on the dynamic and disordered nature of these sites during the course of experiments $^{38-44}$ or the isolated nature of VO_x in the octahedral arrangement of MoO_x groups. 45 In contrast, measurements on M1-phase samples of different crystallite sizes have shown that C₂H₆ ODH rates depend on micropore volumes and not on external surface areas, suggesting that reactions instead occur inside the ordered seven-membered ring micropores. 46 DFT studies on M1-phase oxides of MoVTeNb and MoVO forms have probed the arrangements of framework V and Mo atoms and effects of proximity of V centers on the stability of the oxide 27,47,48 and reactivity of different sites in cluster and periodic models via calculations of C–H activation energies or reactivity descriptors such as H atom addition energy to the O atoms. $^{27,30,48-53}$ Terminal V= O O atoms, V-O-Mo bridging O atoms, and terminal Te=O atoms have been suggested as the most active sites, and the reactivity of Te=O sites is shown to be enhanced by vicinal Voxo species. ^{27,30,48–53} These studies have not probed the role of pores of the M1-phase oxides and are essentially restricted to analyses of C-H activation or ammoxidation steps; steps limiting the selectivity to dehydrogenated products have not been performed.

Our recent measurements showed that ODH rate ratios of C_2H_6 to cyclohexane (C_6H_{12}) on M1 catalysts are up to 2 orders of magnitude larger than ratios measured on vanadium oxides and ratios derived from DFT at identical active sites at outer surfaces in the M1 phase.⁵⁴ Since the size of C_2H_6 is

sufficiently small but that of C₆H₁₂ is too large to enter the seven-membered ring micropores of MoVTeNb oxides and vanadium oxides do not contain such well-defined micropores to exclude C₆H₁₂, these molecular size-dependent rate data confirm that C₂H₆ activation occurs predominantly inside the micropores. Differences between C₂H₆ and C₆H₁₂ activation enthalpies on M1 oxides and vanadium oxides without micropores, and DFT calculations suggested that C₂H₆ transition states inside the tightly confined pores are stabilized significantly by van der Waals (vdW). The high C₂H₄ selectivity in these oxides was attributed to this vdW stabilization for C-H activation and steric hindrance to undesired C-O bond formation steps inside the tight pores, 54 without the determination of kinetic parameters relevant to selectivity and rigorous comparison of such parameters on different types of O atom species accessible on external surfaces. These molecular size-dependent kinetic probes and DFT-based analyses and proposals about the role of pores suggest that selectivity in alkane oxidation, which were earlier considered from the perspective of elemental composition and corresponding electronic properties of catalysts, can also be modified by structures and sizes of confining voids.

Here, we use DFT to analyze structural and reactive properties of different types of lattice O atoms in V₂O₅(001) and MoVTeNbO catalysts. Plausible steps that activate C-H bonds in C₂H₆ and form oxidation products from C₂H₅ radicals and C2H4 molecules are calculated and compared on O atoms involved in three different catalyst models (i) on a two-layer V₂O₅(001) surface, (ii) inside MoVTeNbO sevenmembered ring pores, and (iii) on one-layer MoVTeNbO(001). These calculations and mole balance analysis for the effects of C₂H₆ conversion on measured C₂H₄ selectivity are used to define kinetic parameters relevant to selectivity and establish which DFT-derived activation barrier differences are relevant to measured kinetic parameters. The disparate effects of subsurface oxide on C-H activation and C-O bond formation barriers are also analyzed. We show that the preference for forming epoxide over acetaldehyde from C₂H₄ on M=O terminal O atoms is greater than that on bridging M-O-M O atoms, which changes the identity of transition states relevant to selectivity on these different types of lattice oxygens. Tri-coordinated V2-O-V and bridging V-O-V and V-O-Mo O atoms are more resistant to oxidation of C₂H₄ than the terminal O atoms. The absence of accessible terminal O atoms as well as the tight-confinement effects contributes to the high C₂H₄ selectivity in pores of MoVTeNbO. The H atom addition energies at the lattice O atoms, van der Waals components of interaction between molecules and solids, and energies of distortion of crystalline framework of the catalyst to accommodate transition states are determined to be important energy-based descriptors that explain the effects of O atom coordination as well as pore confinement effects on wide varieties of lattice O atoms.

2. METHODS

2.1. Computational Methods. Periodic density functional theory (DFT) calculations for C_2H_6 and C_2H_4 conversions on M1-phase MoVTeNb oxides and V_2O_5 oxides were carried out using Vienna ab initio Simulation Package (VASP). Exchange correlation functionals based on generalized gradient approximation with empirical van der Waals corrections included within the functional (vdW-DF2)^{58,59} and without such corrections (PBE)⁶⁰ were employed. Plane-wave basis

sets used to approximate wave functions of valence electrons were included up to a 400 eV kinetic energy cut-off. The interactions of valence electrons with atom cores were described by the projector augmented wave method.⁶¹ All calculations were spin-polarized. Gaussian smearing was imposed for electron distributions near the Fermi level (widths of 0.02 eV for MoVTeNbO and 0.01 eV for V2O5), and energies were extrapolated to zero smearing. The differences between the numbers of spin-up and spin-down electrons were not specified for the results reported here, but the effect of specifying these values to singlet, triplet, and quintet multiplicities on some calculations including bare catalyst, C-H bond activation, and C-O bond formation transition states was tested and found to be less than 5 kJ mol⁻¹ (Section S1, Supporting Information). The spin multiplicities for all intermediates and transition states and spin distribution maps for some are also shown in Tables S5, S7, and S9 and Figures S12 and S13 (Supporting Information). The DFT + U method was not used because the Hubbard U interactions tend to result in lower H abstraction barriers than experiments for model metal oxide systems.⁶² The electronic structure was converged until the difference in energies between successive steps was less than at least 1×10^{-5} eV. Geometries of reactive intermediates and transition states were optimized until the forces on atoms were less than 0.05 eV.

The $V_2O_5(001)$ surface was simulated using a two-layer slab model with 12 V atoms and 30 O atoms in each layer and a 11.16 Å vacuum gap between bilayers in the [001] direction. The size of this supercell for this model was $11.64 \times 10.81 \times$ 20.00 Å³, which was determined by relaxing the bulk V_2O_5 lattice using PBE functional (details in Section S2, Supporting Information). A unit cell for the M1 phase contains 28 Mo, 8 V, 4 Te, 4 Nb, and 116 O atoms in each layer of the layered oxide used in this work. 47,53 The model for bulk M1-phase oxides consists of two identical layers along the [001] direction without a vacuum gap between layers, leading to 21.37 × 26.94 \times 8.12 Å³ orthorhombic supercells. These dimensions were determined by choosing a unit cell from crystallographic measurements 45 and relaxing it symmetrically to determine the size that leads to the most negative energy per unit cell for PBE functional (details in Section S2, Supporting Information). The location of Mo, V, Te, and Nb atoms in the unit cell was chosen from the most stable configurations determined in a previous computational study.⁴⁷ This computational work screened a large number of possible V locations to determine the tendency of V atoms to be dispersed within the MoO_x framework and exhibited reasonable consistency with interpretations of V atom distributions from Z-contrast measurements in atom-resolved microscopy and Rietveld refinement studies. 30,47,63,64 A second model used to represent the MoVTeNbO(001) surface consists of a supercell with one layer of the M1-phase unit cell and a vacuum region of 10.94 Å along the [001] direction to separate the layers for access to reactants, leading to supercell dimensions of 21.37 × 26.94 × 15.00 Å³. Effects of adding a second layer to the MoVTeNbO(001) model on steps most relevant to selectivity were probed using a $21.37 \times 26.94 \times 19.06 \text{ Å}^3$ supercell shown in Figure S2 (Supporting Information).

The first Brillouin zone was sampled using $2 \times 2 \times 1$, $1 \times 1 \times 2$, and $1 \times 1 \times 1$ Monkhorst-Pack k-point meshes⁶⁵ for $V_2O_5(001)$, MoVTeNbO pores, and MoVTeNbO(001), respectively, based on relative supercell dimensions and direction of the vacuum region. The atomic arrangements

and bond distances are described in more detail in Section 3.1. The long-range interactions among neighboring slabs for $V_2O_5(001)$ and MoVTeNbO(001) models were corrected using dipole moments along the [001] direction and by subtracting the classical dipole interactions among these layers from the calculated DFT energies. The nudged elastic band method was used to determine minimum energy paths connecting reactants and products along the potential energy surface (PES). The structures near the maxima on these paths were then used to calculate transition states using the dimer method. 68

Enthalpies, entropies, and Gibbs free energies were determined using the electronic energies derived from DFT and the ideal gas statistical mechanics formalisms (details in Section S3). Vibrational frequencies were obtained via diagonalization of Hessians generated from two-sided finite differences of energy gradients obtained by perturbing each atom by 0.01 Å in Cartesian directions of optimized structures.⁶⁹ Such perturbations were performed for all atoms of reactive molecular species and for one and two transition metal atoms (M) for reactions at the M=O terminal atom and M-O-M bridging O atom, respectively, along with the terminal or bridging O atoms involved in the reactions. Contributions from low-frequency vibrational modes, which lead to significant errors in enthalpy and entropy values, were replaced by a fraction (0.7) of the translational and rotational values from relevant gas-phase molecules.⁷⁰ Low frequencies were taken to be 100 cm⁻¹ for steps involving C-O bond formation and 60 cm⁻¹ for other steps because these cutoffs lead to entropy differences between the kinetically relevant transition states that closely match measured C₂H₄ selectivities on V₂O₅ and were kept consistent for all catalyst models. Rate constants were determined using the Eyring-Polanyi equa-

$$k = \frac{k_{\rm B}T}{h} \exp\left(-\frac{\Delta G^{\neq}}{RT}\right) = \frac{k_{\rm B}T}{h} \exp\left(\frac{\Delta S^{\neq}}{R}\right) \exp\left(-\frac{\Delta H^{\neq}}{RT}\right) \tag{1}$$

where T is the temperature, k is the rate constant, $k_{\rm B}$ is the Boltzmann constant, h is the Planck constant, and R is the universal ideal gas constant. ΔG^{\neq} , ΔS^{\neq} , and ΔH^{\neq} represent Gibbs free energy, entropy, and enthalpy differences between transition state and relevant precursor, respectively.

2.2. Experimental Methods and Catalyst Characterization. A brief description of the procedures used for the synthesis and characterization of catalyst samples and rate measurements is provided here; more detailed descriptions can be found elsewhere.⁵⁴ A supported vanadium oxide catalyst was prepared by adding SiO₂ powder to an aqueous solution with 1:1.5:100 oxalic acid/ammonium metavanadate/H₂O molar ratios under continuous stirring on a hot plate, drying the resulting slurry at 373 K for 2 h in an oven, and treating the solids in flowing air in a tube furnace ramped to 873 K at 0.083 K s⁻¹ and held for 6 h. This procedure led to VO_x/SiO₂ samples with 41 wt % of V₂O₅, which corresponds to a high theoretical surface density of 9.6 V nm⁻² based on the surface area of the SiO₂ powders used.⁵⁴ XRD measurements, however, showed that samples contained V2O5 crystals and possibly much smaller amounts of more dispersed VO_x domains. 54 The surface area of VO_x/SiO₂ samples determined from multipoint Brunauer-Emmett-Teller (BET) analysis was 35.3 m² g⁻¹. Unsupported V₂O₅ samples were also prepared to detect if the presence of dispersed VO_x domains significantly modified the kinetic parameters on 41 wt % VO_x SiO₂ samples. These samples were prepared by treating ammonium metavanadate in flowing air (50 cm³ min⁻¹) in a tube furnace heated to 773 K at 0.083 K s⁻¹ and held for 3 h. The XRD measurements in these samples showed orthorhombic V_2O_5 crystals, and the BET surface area was 8.1 m² g⁻¹. The measurements of rate constant ratios relevant to C_2H_4 selectivity on V_2O_5 and comparisons to 41 wt % VO_x/SiO_2 are shown in Section S19 (Supporting Information); these data suggest similar values of rate constant ratios in the two types of samples.

MoVTeNbO samples were prepared by hydrothermal treatment of aqueous solution of ammonium molybdate tetrahydrate, vanadyl sulfate, telluric acid, and ammonium niobate oxalate hydrate with 1:0.25:0.17:0.12 Mo/V/Te/Nb atomic ratios in a sealed Teflon vessel inside a stainless steel autoclave at 448 K for 48 h. The solid products were collected from the vessel, washed with deionized water, and dried overnight in an oven at 373 K. The dried solids were treated in flowing helium in a tube furnace ramped to 873 K at 0.083 K s⁻¹ and held for 2 h to form final products. The internal area of seven-membered ring micropores considered to be cylinders of 0.4 nm diameters and the external surface area of MoVTeNbO samples, determined from N2 physisorption measurements and BET analysis, was 7.9 and 4.2 m² g⁻¹, respectively.⁵⁴ These samples contained 1:0.27:0.02:0.09 Mo/V/Te/Nb atomic ratios as determined using inductively coupled plasma atomic emission spectroscopy. X-ray diffraction (XRD) measurements exhibited peak positions consistent with the crystal structure of the M1 phase, along with minority M2 and M5O14 phases that do not contain pores large enough for ethane to enter.⁵⁴ The samples showed a plate- and rod-like morphology upon inspection under a scanning electron microscope. 54 Alternative MoVTeNb sample preparations with near-complete purity of the M1 phase as well as M1-phase MoV samples were prepared. 54,74 These alternative catalysts lead to similar values of rate constant ratios relevant to C2H4 selectivity as the sample described here.⁷

Rate and selectivity measurements for C_2H_6 - O_2 reactions were carried out on pressed, crushed, and sieved catalyst samples with $106-180~\mu m$ aggregate sizes in a U-tube quartz reactor with plug-flow hydrodynamics and electronic control for temperature and flow rates of gases. The reactor effluents were analyzed using a gas chromatograph equipped with a carboxen-1000 packed column and an HP-PLOT Q capillary column and with thermal conductivity and flame ionization detectors. The effect of C_2H_6 conversion on rates and C_2H_4 selectivity was measured at isothermal conditions at different temperatures (648 to 733 K, 3 or 5 kPa C_2H_6 , 3 or 5 kPa O_2 , balance He). Samples were heated to reaction temperatures at 0.25 K s⁻¹ in flowing helium prior to the introduction of reactants.

3. RESULTS AND DISCUSSION

3.1. Structures and Reactivity of O Atoms in V₂O₅ **and MoVTeNbO Models.** *3.1.1. Atomic Arrangements, Bond Distances, and Interlayer Distances.* Optimized structures and bond distances in models used to represent VO_x/SiO_2 and MoVTeNbO catalysts are shown in Figure 1. The VO_x/SiO_2 samples are represented by the most stable (001) surfaces of orthorhombic V_2O_5 crystals^{32,33} because a high V loading sample was used and this phase was detected in XRD

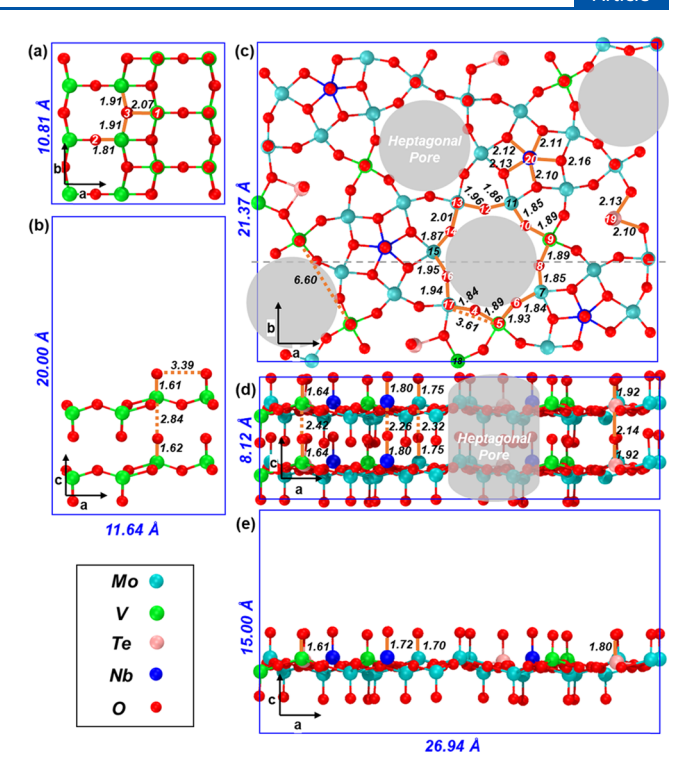


Figure 1. (a) Top view and (b) side view of the $V_2O_5(001)$ surface, (c) top view of MoVTeNbO, (d) side view of bulk MoVTeNbO with two layers in the supercell, and (e) side view of one-layer MoVTeNbO(001) surface. Side views in (d) and (e) show cross sections at the dashed gray line in (c). Gray circles and cylinders represent heptagonal pores. O atom sites are labeled by serial numbers 1–3 for O atoms in V_2O_5 and 4–20 for O atoms in MoVTeNbO (O atoms at locations 7, 11, 15, and 18 are under the labeled metal atoms).

measurements.⁵⁴ This oxide contains layers of interconnected distorted V-oxo octahedra with terminal (V=O), bridging (V-O-V) and tri-coordinated (V_2-O-V) O atoms labeled 1, 2, and 3, respectively, in Figure 1a. The terminal O atoms are much closer to V atoms in one layer (V=O bond distance of 1.61 Å, Figure 1b) than the adjacent layer (2.84 Å, Figure 1b), consistent with the absence of covalent bonding between the layers that are held together by van der Waals (vdW) interactions. The distances of bridging O atoms to two V atoms are 1.81 Å each, while the tri-coordinated O atoms have a 1.91 Å distance from two V atoms and 2.07 Å from a third O atom (Figure 1a). The distance between O atoms in nearest pair of identical V=O terminal bonds is 3.39 Å (Figure 1b). The V-O distances in the bulk V₂O₅ model were 1.61 and 1.79 Å for V=O and V-O-V sites, respectively, while the distances involved in V₂–O–V are 1.90 and 2.04 Å, suggesting that no significant changes in structural parameters occur when bulk oxide is cleaved to create surfaces. The surface energy determined from electronic energy differences between bulk and surface models is 0.172 J m⁻², which is about an order of magnitude smaller than typical surface energies of most stable surfaces of precious metals such as Pt(111) and indicates small energy penalties for disrupting interlayer vdW interactions to create surfaces.⁷⁵

The framework of the M1 phase for the mixed oxides consists of layers of distorted octahedra of Mo- and V-oxo species, in which Nb and Te atoms preferentially occupy pentagonal and hexagonal rings, respectively. The numbers

of V and Mo framework atoms used here correspond to a V/ Mo ratio of 0.29, which is similar to the 0.27 ratio determined from elemental analysis of the catalyst samples used in kinetic measurements. The locations of framework V atoms in the model used here were chosen based on the most stable sites identified in a previous computational study, 47 which leads to a structure with many distinct types of terminal, bridging, and tri-coordinated O atoms, some of which are labeled 4 to 20 in Figure 1c. For the optimized structure of the bulk oxide, the O atom distances from metal atoms in terminal V=O, Mo=O, and Nb=O bonds are 1.64, 1.75, and 1.80 Å, respectively (Figure 1d). The differences among these distances are consistent with trends in ionic radii of V⁵⁺, Mo⁶⁺, and Nb⁵⁺ ions.⁷⁷ The respective distances of the terminal O atoms from V, Mo, and Nb atoms in the adjacent layers (2.42, 2.32, and 2.26 Å, respectively, Figure 1d) are much larger than those of the M=O bonds but shorter than corresponding distances in V_2O_5 (2.84 Å), which suggests that these oxides have shorter separations and stronger interactions between layers. The O atoms connecting Te atoms have even less asymmetric distances of 1.92 and 2.14 Å from atoms in two adjacent layers, consistent with the formation one-dimensional Te-O-Te-O chains that lead to some covalent bonding across layers. The bridging O atoms within a layer consist of V-O-Mo and Mo-O-Mo bridges with V-O and Mo-O distances ranging from 1.8 to 2.1 Å (Figure 1c). The Nb and Te atoms in the rings exhibit 2.1–2.2 Å distances from bridging O atoms (Figure 1c).

MoVTeNbO(001) surfaces are formed by the separation of layers at vdW contacts for terminal O atoms of other cations and the disruption of longer of the two types of covalent bonds in Te-O-Te-O chains. This separation decreases the shorter Te-O bond distances to 1.80 Å in Te=O in the (001) surface model from 1.92 Å in the bulk oxide (Figure 1e). The terminal V=O, Mo=O, and Nb=O bond distances exhibit a more modest decrease to 1.61, 1.70, and 1.72 Å from 1.64, 1.75, and 1.80 Å, respectively. The surface energy for the MoVTeNbO(001) plane is 0.251 J m⁻², which is larger than $V_2O_5(001)$ despite the less dense porous structure of the layers because O atoms in the M1-phase oxides exhibit greater interlayer interactions. The one-layer (001) surface with vacuum resembles periodic surface models previously used to represent M1-phase catalysts²⁷ but with different specific locations of V atoms in the framework. The absence of additional layers below the (001) surface in such models may introduce artifacts in reactivity at Te=O sites due to disruption of the interlayer covalent bonding but may cause less significant disruptions for other terminal O atoms due to their longer distances from the next layer in the bulk oxide. The Te sites in M1 catalysts decrease in concentrations during reactions, which does not influence the ODH rate over long reaction times, 41,79,80 suggesting that their disruptions caused only minor changes to catalytic properties or relevant active sites. The terminal O atom nearest to V=O is a Mo=O site with a distance of 3.61 Å, much larger than the 3.39 Å distance between V=O pairs in $V_2O_5(001)$ (Figure 1b,c). The nearest V=O pair O atom distance in MoVTeNbO is 6.60 Å (Figure 1c).

3.1.2. H Atom Addition Energy (HAE) at Lattice O Atoms. Lattice O atoms with stronger H abstraction strength (i.e., more negative HAE) tend to be more reactive for C–H bond activation because activation energies exhibit Brønsted–Evans–Polanyi-type near-linear dependence on reaction energies for elementary steps. 21,62,81,82 HAE values also often

correlate with O atom removal energies relevant to C–O bond formation reactions because both H addition and O removal depend on the band gap and energies required to place electrons in empty d-bands. 83–85

HAE values for some types of O atoms on V₂O₅ and MoVTeNbO derived from vdW-DF2 are shown in Table 1,

Table 1. vdW-DF2-Derived HAE Values (without Zero-Point Energy Corrections) in $\rm V_2O_5$ and MoVTeNbO at Different O Atom Locations in Figure 1

	HAE (kJ mol ⁻¹)			
O atom location	V ₂ O ₅ (001)	MoVTeNbO pores	MoVTeNbO(001)	
1	-286			
2	-273			
3	-275			
4		-256	-269	
5		-241	-254	
19		-267	-309	
20		-231	-257	

while those for a more complete set of sites along with comparisons to PBE and PBE-D3BJ⁸⁶ methods are shown in Tables S2-S4 (Supporting Information). The vdW-DF2derived HAE at V=O sites of $V_2O_5(001)$ is -286 kJ mol⁻¹ (site 1, Figure 1a; Table 1), which represents a significantly stronger H abstraction strength than V-O-V and V2-O-V sites (HAE values of -273 and -275 kJ mol⁻¹ for sites 2 and 3, Figure 1a). This suggests that the terminal O atoms are the most reactive sites on $V_2O_5(001)$. The vdW-DF2-derived HAE values for terminal and bridging O atoms of MoVTeNbO(001) located at the heptagonal pores (sites 4 to 17, Figure 1c) range from -203 to -269 kJ mol⁻¹ (Table S3). The HAE among these sites is most negative for a V-O-Mo bridgebonded O atom (-269 kJ mol⁻¹, Table 1; site 4, Figure 1c) and less negative for a vicinal V=O O atom $(-254 \text{ kJ mol}^{-1})$ Table 1; site 5, Figure 1c), suggesting that bridge-bonded O atoms are more reactive than terminal O atoms in M1-phase catalysts. The more negative HAE at bridge-bonded O atoms than terminal O atoms is consistent with recent hybrid-DFT and DFT + U studies on M1-phase MoVO oxides without Te and Nb elements. 48 The vdW-DF2-derived HAE values for V-O-Mo and V=O O atoms in the MoVTeNbO bulk model at sites 4 and 5 are -256 and -241, respectively. The bulk models exhibit less negative absolute values than the (001) models but similar relative values for different types of sites near the heptagonal ring. The HAE values for Nb=O O atoms in M1-phase models are less negative than V-O-Mo sites (Table 1), suggesting that these species do not contribute significantly to reactivity. The HAE for Te-O sites are substantially less negative in bulk than in the (001) model (HAE values of -267 and -309 kJ mol⁻¹ in pores and (001), which represent the artificial nature of the Te=O species formed by cleavage of -Te-O-Te-O- chains. The Te sites preferentially located in the smaller six-membered rings are inaccessible to reactants in the bulk and unstable at surfaces in ODH conditions. 41,79,80 The mobility of Te atoms have been suggested to be linked to reactivity of MoVTeNbO oxides, but Te elusion from the crystals has also been correlated to decomposition of the oxide to denser phases, 79 which links it to stability rather than reactivity and selectivity. We previously considered the possible role of Te=O sites in ethane activation by comparing measured ethane/cyclohexane rate

The Journal of Physical Chemistry C

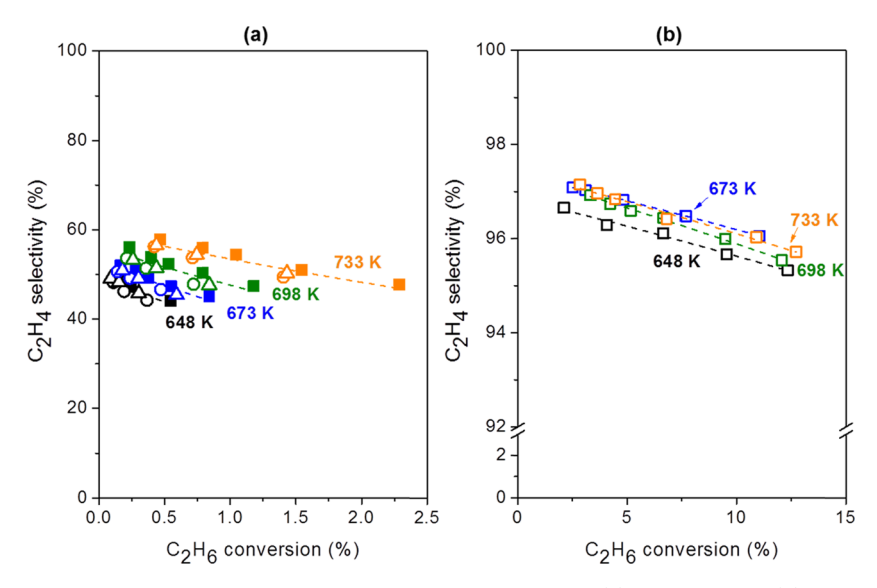


Figure 2. Measured C_2H_4 selectivities in C_2H_6 -O₂ reactions as a function of conversion on (a) VO_x/SiO_2 and (b) MoVTeNbO at different reactant pressures (3 kPa C_2H_6 and 3 kPa O_2 , squares; 3 kPa O_2 , circles; 5 kPa O_2 , circles; 5 kPa O_2 , triangles) and temperatures (648 K, black; 673 K, blue; 698 K, green; 733 K, orange). Dashed curves represent best fits to the form of eq 6.

ratios on MoVTeNbO to DFT-derived values determined on Te=O sites. Such ratios were predicted to be 2×10^{-3} based on DFT, but the measured values were near unity, which suggested that Te=O sites cannot account for the measurements and most of ethane activations instead occur inside the pores. In this work, we have compared the selectivity at Te=O sites to other sites and found that these Te=O sites will lead to lower selectivity than the V-O-Mo sites inside the pores, as shown in Section S20 (Supporting Information). HAE values for PBE and PBE-D3BJ methods show small differences but same general trends as the vdW-DF2 (Tables S2-S4).

These structural details and HAE values reveal that active sites in V₂O₅ are stronger H abstractors than M1-phase oxides and that the terminal O atoms are the strongest H abstractors in $V_2O_5(001)$ (HAE = -286 kJ mol⁻¹ at site 1, Figure 1), while bridging O atoms are stronger abstractors in pores of MoVTeNbO (HAE = -256 kJ mol⁻¹ at site 4). The elementary steps for conversion of C2H6 and C2H4 via C-H activation and C-O formation were probed at both terminal and bridging O atoms using HAE as a guidance for most reactive sites but also considering the different extent of steric hindrances or radical-surface interactions²¹ that may stabilize the transition state to different extent than trends predicted solely from HAE. Reactions on $V_2O_5(001)$ were probed on the V=O terminal atoms (site 1, Figure 1a), and some comparisons were made with the V-O-V bridging O atom. On MoVTeNbO surface and pore models, these steps were calculated on V-O-Mo bridging O atoms (site 4, Figure 1c) as well as the V=O terminal O atoms (site 5, Figure 1c). Next, we describe measured rate constant ratios relevant to selectivity, which are then compared with DFT calculations for the models described here.

3.2. Measured Rate Constant Ratios and Activation Barrier Differences Relevant to C_2H_4 Selectivity. The effects of reactant pressure and temperature on C_2H_6 and C_6H_{12} oxidation rates and selectivity on the 41 wt % VO_x/SiO_2 samples and the MoVTeNbO samples with minority impurity phases without heptagonal channels were measured and reported previously. Standard Unsupported V_2O_5 and MoO $_3$ samples, 1.5 wt % VO_x/SiO_2 , 11% VO_x/SiO_2 , and essentially pure forms

of M1-phase MoVTeNbO and M1-phase MoVO catalysts were also prepared, and analogous rate and selectivity measurements were performed.⁷⁴ In all these catalysts, the ethane conversion rates are in the first order in ethane pressure and zero order in O2 pressure, consistent with kinetic details typical of alkane dehydrogenation via Mars-van Krevelen cycles. All VO_x/SiO₂, V₂O₅, and MoO₃ samples lead to C₂H₆/ C_6H_{12} activation rate ratios much less than unity (below 0.025 at 3 kPa C₂H₆ or C₆H₁₂, 3 kPa O₂ and 648 K) when normalized by the same number of active sites for both hydrocarbons⁷⁴ because reactions are mediated by C–H activations and C₆H₁₂ has weaker C-H bonds than C₂H₆, leading to higher rates in the denominator. 54 The low C₂H₆/ C₆H₁₂ ratios are consistent with DFT-derived activation energies and rate constants predicted at 648 K for both molecules activating on the same O atom, irrespective of the type of O atom used.⁵⁴ In contrast, rate ratios measured on M1-phase MoVTeNbO or MoVO samples exhibit C₂H₆/ C₆H₁₂ activation rate ratios near unity and up to 2 orders of magnitude higher than oxides without micropores. Since heptagonal pores in the M1 phase have nearly the same accessible diameter as the size of ethane molecule but restrict larger molecules, these rate ratios measured on several types of oxides and the DFT calculations provide a strong evidence that most of the initial ethane activations in M1-phase catalysts occur primarily inside the micropores. The heptagonal pores stabilize C₂H₆ molecules by van der Waals interactions, leading to high reactivity in pores even with small amounts of accessible pores.⁵⁴

Electron microscopy and Rietveld refinement studies suggest that the occupation of the metal positions in the M1 crystal structure is somewhat variable and some heptagonal pores are occupied by metal cations. ^{30,63,64} The M1-phase crystallites can exhibit rod- or plate-like shapes with (001) planes containing exposed heptagonal pores on the ends but different types of planes exposed on the sides of the crystallites. ¹³ While many studies propose (001) planes to be the most relevant to reactivity, ^{45,88,89} some correlations are observed between the shape and measured rates that are proposed to originate from the types of exposed facets. ¹³ Some of these structural

differences can indeed affect reactivity of the catalysts. For instance, crystallites of different shapes may also have different extent of accessible pores, and samples with partial blockage of heptagonal pores with cations can lead to lower rates. M1phase samples of different types, despite these rate differences. exhibit similar high C2H4 selectivity in C2H6 oxidation at similar conversion and temperature; this selectivity is much higher than other VOx or MoOx domains, suggesting that external exposed facets and differences in occupation positions of elements cannot explain the observed selectivity and some property of the M1-phase crystal structure itself is relevant. Microscopy studies also propose that formation of radical-type oxygen around Te site MoVTeNb oxides is relevant to activity and selectivity. 80 Yet, MoVO samples without Te also exhibit similar high selectivity and similar values of ratios of rate constants for desired and undesired reactions relevant to selectivity.⁷⁴ Furthermore, none of the structural differences for external facets explain or contradict the high C₂H₆/C₆H₁₂ rate ratios in the M1 phase that strongly suggest C2H6 reactions occurring inside pores restrictive to C₆H₁₂ because different types of exposed planes should lead to low C2H6/C6H12 rate ratios due to weaker C-H bonds in C₆H₁₂ but fully formed heptagonal pores restrict C₆H₁₂. ⁵⁴ Thus, comparison of very similar measured selectivity parameters representative of essentially all M1-phase catalysts, despite differences in rates, elemental distribution, or external surfaces, to the DFT-derived selectivity parameters on a representative M1-phase model seems reasonable. Here, instead of the rate differences, we focus on the effects of C₂H₆ conversions on C₂H₄ selectivities and use these measurements to extract ratios of rate constants relevant to selectivity.

3.2.1. Extraction of Rate Constant Ratios from Measured Selectivity Data. The C₂H₄ selectivity as a function of C₂H₆ conversion for different residence times measured on VO_x/ SiO₂ and MoVTeNbO catalyst samples at various C₂H₆ and O₂ pressures and temperatures (648-733 K) are shown in Figure 2. For the VO_x/SiO₂ catalyst, higher temperatures lead to higher selectivity at zero conversion (50-60%) and less sensitive decrease in selectivity with conversion (Figure 2a). For the same conditions, MoVTeNbO catalysts exhibit selectivities at zero conversion much higher than VO_x/SiO₂ (>95%) and much less sensitive to conversion and temperature (Figure 2b).

A sequence of product formation convenient for analyzing reaction paths relevant to C₂H₄ selectivity in C₂H₆ oxidative conversion is shown in Scheme 1a. Here, the formations of C₂H₄ and of oxygenated products directly from a primary C-

Scheme 1. (a) Lumped Rate Constants and (b) Gibbs Free Energies for Steps Involved in Oxidative Conversion of C₂H₆ to C₂H₄ and Oxygenated Products

(a)
$$C_2H_6 \xrightarrow{k_1} C_2H_4$$

 $k_2 \xrightarrow{k_3} CO, CO_2$
(b) $C_2H_6 \xrightarrow{\Delta G_1} C_2H_5 \xrightarrow{\Delta G_1'} C_2H_4$
 $\Delta G_2 \xrightarrow{\Delta G_3} CH_3CH_0, CH_3CH_2OH$

H activation are represented by reaction rate constants k_1 and k_2 , respectively, each with a first-order C_2H_6 pressure dependence and no O₂ pressure dependence. The sequential formation of oxygenated products from C2H4 is described by reactions with a rate constant k_3 and first-order C_2H_4 pressure dependence and no O₂ pressure dependence. These firstorder rate constants represent an ensemble average over possible pathways that lead to the alkene and the undesired products, which are analyzed later using DFT. The selectivities shown in Figure 2 exhibit weak dependence on feed alkane and O_2 pressure. Since measured rates for $\mathrm{C}_2\mathrm{H}_6$ activation exhibits first- and zero-order dependence on C2H6 and O2 pressures, respectively,⁵⁴ this absence of the effect of these pressures on selectivity is consistent with the assumption that parallel and sequential conversion steps in Scheme 1a also have the same pressure dependences as the primary step. The rates of formation of C_2H_6 ($r_{C_2H_6}$), C_2H_4 ($r_{C_2H_4}$), and oxygenated products (r_{CO} , representing final products CO and CO₂ for sequential oxygenation) are given by

$$\frac{r_{C_2H_6}}{[L]} = -k_1 p_{C_2H_6} - k_2 p_{C_2H_6} \tag{2}$$

$$\frac{r_{C_2H_4}}{[L]} = k_1 p_{C_2H_6} - k_3 p_{C_2H_4}$$
(3)

$$\frac{r_{\text{CO}_x}}{[L]} = k_2 p_{\text{C}_2\text{H}_6} + k_3 p_{\text{C}_2\text{H}_4} \tag{4}$$

where [L] is the concentration of active lattice O atoms, and p_{C,H_6} and p_{C,H_4} are pressures of C_2H_6 and C_2H_4 , respectively. A mole balance for the change in the concentration of each species with C₂H₆ residence time, assuming that rates have zero-order dependence on O₂ pressure, leads to the following expressions for C₂H₄ selectivity at zero C₂H₆ conversion $(S_{C,H_{\iota}}^{0})$

$$S_{C_2H_4}^0 = \frac{k_1}{k_1 + k_2} = \frac{1}{1 + \frac{k_2}{k_1}} \tag{5}$$

and selectivity (S_{C,H_4}) at finite values of C_2H_6 conversion (X)(derivation in Section S5, Supporting Information)

$$S_{C_2H_4} = \frac{S_{C_2H_4}^0}{\left(1 - S_{C_2H_4}^0 \frac{k_3}{k_1}\right)} \left[\frac{(1 - X)^{S_{C_2H_4}^0 \frac{k_3}{k_1}} - (1 - X)}{X} \right]$$
(6)

For low conversions, where 1 - X can be approximated as 1, eq 6 is simplified to

$$S_{C_2H_4} = S_{C_2H_4}^0 \left(1 - \frac{1}{2} S_{C_2H_4}^0 \frac{k_3}{k_1} X \right)$$
 (7)

Measured S_{C₂H₄} values decrease with increasing conversion (Figure 2), and eqs 5-7 suggest that intercepts and slopes at low conversion for selectivity versus conversion plots depend solely on rate constant ratios. Higher selectivity at zero conversion and smaller decrease in selectivity with increasing conversion correspond to smaller values of k_2/k_1 and k_3/k_1 ,

Regression of selectivity data in Figure 2 to the form of eqs 5 and 6 was used to derive k_2/k_1 and k_3/k_1 values shown as a function of reciprocal temperature in Figure 3. The k_2/k_1 and k_3/k_1 values on 41 wt % VO_{ν}/SiO₂ catalysts are in ranges of

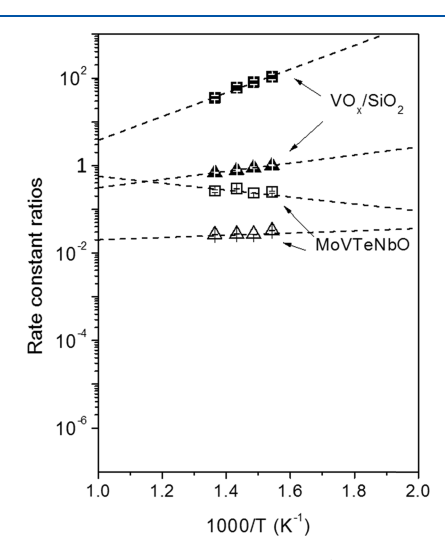


Figure 3. Measured rate constant ratios (k_2/k_1) , triangles; k_3/k_1 , squares) as a function of reciprocal temperature on VO_x/SiO₂ (closed symbols) and MoVTeNbO (open symbols). Dashed lines represent best fits to the forms of eqs 8 and 11. Error bars represent the standard error.

1.0-0.7 and 110-36, respectively, for measurements at 648-733 K (Figure 3). These k_3/k_1 values are about 2 orders of magnitude larger than k_2/k_1 , suggesting that sequential reactions of C₂H₄ contribute to the lowering of C₂H₄ selectivity much more significant than the parallel oxygenate formations from C₂H₆ at all conversions greater than about 1%. Both ratios decrease with temperature, consistent with higher selectivity at higher temperatures and with lower activation enthalpies for oxygenate formation steps than the ODH steps. The k_3/k_1 and k_2/k_1 values on unsupported V_2O_5 samples were measured at different temperatures, as shown in Section \$19 (Supporting Information); these values lie on the trend lines for VO_x/SiO₂, suggesting no significant differences in selectivity because both samples contain significant V₂O₅ crystals. On MoVTeNbO catalysts, k_2/k_1 and k_3/k_1 values are in ranges of 0.032-0.026 and 0.23-0.29, respectively, for measurements at 648-733 K (Figure 3). These values are 2 orders of magnitude smaller than VO_x/SiO₂ catalysts, consistent with much higher selectivity in M1-phase materials. The MoVTeNbO oxide also exhibits k_3/k_1 values larger than k_2/k_1 values, which suggests more significant selectivity limitations due to sequential reactions. The k_3/k_1 for MoVTeNbO are insensitive to temperature (Figure 3), which suggests that the ODH steps and the sequential oxygenate formation steps have similar activation enthalpies, which contrasts the temperature dependences for V₂O₅ and other redox catalysts that exhibit lower activation energies for

the latter steps. The k_2/k_1 and k_3/k_1 values measured at 648 K on phase-pure MoVTeNb oxides and on MoVO samples without Te or Nb are very similar to those on the MoVTeNbO samples examined in Figure 3 and much lower than those on VO_v/SiO₂. ⁷⁴

3.2.2. Dependence on Rate Constant Ratios on Gibbs Free Energy Differences. The rate constants relevant to C_2H_6 ODH rates and selectivity in Scheme 1a depend on Gibbs free energies of steps shown in Scheme 1b. The activation of C_2H_6 via Mars—van Krevelen redox cycles invariably requires an initial irreversible homolytic C—H bond activation at lattice O atoms to form $\cdot C_2H_5$ radical species, 28,31 which is shown in Scheme 1b as a step with Gibbs free energy activation barrier ΔG_1 . These radicals can directly undergo second C—H activation to C_2H_4 or form a C—O bond at lattice O atoms to complete the steps for C_2H_4 or oxygenate formation. Therefore, the k_2/k_1 rate constant ratios depend on the difference between the free energy barriers for oxygenate and C_2H_4 formations from a $\cdot C_2H_5$ radical (ΔG_2 and $\Delta G_1'$, Scheme 1b), as shown by the following expression

$$\frac{k_2}{k_1} = \frac{\frac{k_B T}{h} \exp\left(-\frac{\Delta G_2}{RT}\right)}{\frac{k_B T}{h} \exp\left(-\frac{\Delta G_1'}{RT}\right)} = \exp\left(-\frac{\Delta G_2 - \Delta G_1'}{RT}\right)$$
(8)

where the definitions of $k_{\rm B}$, T, h, and R are the same as those in eq 1. Since the first C–H activation in C_2H_6 is typically irreversible, 28,31 we assume that the rate constant representing the total rate of C_2H_6 activation, given by the sum of k_1 and k_2 , depends only on the barrier for the first C–H activation:

$$k_1 + k_2 = \frac{k_{\rm B}T}{h} \exp\left(-\frac{\Delta G_1}{RT}\right) \tag{9}$$

The rate constant k_3 for formation of oxygenates from C_2H_4 depends on Gibbs free energy barrier ΔG_3 in Scheme 1b, leading to k_3/k_1 values given by

$$\frac{k_3}{k_1} = \frac{(k_1 + k_2)}{k_1} \frac{k_3}{(k_1 + k_2)}$$

$$= \left(1 + \frac{k_2}{k_1}\right) \exp\left(-\frac{\Delta G_3 - \Delta G_1}{RT}\right) \tag{10}$$

Substituting for the value of k_2/k_1 from eq 8 gives

$$\frac{k_3}{k_1} = \left(1 + \exp\left(-\frac{\Delta G_2 - \Delta G_1'}{RT}\right)\right) \exp\left(-\frac{\Delta G_3 - \Delta G_1}{RT}\right)$$
(11)

Thus, the rate constant ratios relevant to selectivity depend on two activation energy barrier differences, $\Delta G_2 - \Delta G_1'$ and $\Delta G_3 - \Delta G_1$ described in Scheme 1. The Gibbs free energy differences in eqs 8 and 11 are further expressed as enthalpy and entropy differences ($\Delta G = \Delta H - T\Delta S$), and the measured rate constant ratios in Figure 3 are regressed to the form of the

Table 2. Measured Activation Enthalpy and Entropy Differences between C-H Activations and C-O Formations on VO_x/SiO_2 and MoVTeNbO

	$\Delta\Delta H~(kJ~mol^{-1})$		$\Delta\Delta S~(J~mol^{-1}~K^{-1})$	
model	$\Delta H_2 - \Delta H_1'$	$\Delta H_3 - \Delta H_1$	$\Delta S_2 - \Delta S_1'$	$\Delta S_3 - \Delta S_1$
VO _x /SiO ₂ MoVTeNbO	-18 (±1) -5 (±7)	-44 (±4) 15 (±10)	$-28 (\pm 1)$ $-37 (\pm 11)$	-34 (±6) 10 (±15)

resulting equations to obtain $\Delta H_2 - \Delta H_1'$, $\Delta H_3 - \Delta H_1$, $\Delta S_2 \Delta S_1'$, and $\Delta S_3 - \Delta S_1$ values for VO_x/SiO₂ and MoVTeNbO, as shown in Table 2.

The values of $\Delta H_2 - \Delta H_1'$ and $\Delta S_2 - \Delta S_1'$ are negative for both VO_x/SiO₂ and MoVTeNbO catalysts, which suggests that transition states limiting the rates of parallel oxygenate formation reactions from $\cdot C_2H_5$ in Scheme 1 exhibit lower activation enthalpy than C2H4 formation reaction, but they also lose more entropy. Thus, the undesired parallel reactions are enthalpically favored and entropically disfavored over the C₂H₄ formation steps. The enthalpy contributions decrease with temperature (eq 1), which leads to lower k_2/k_1 values at higher temperatures. The MoVTeNbO samples exhibit ΔH_2 – $\Delta H_1'$ and $\Delta S_2 - \Delta S_1'$ less and more negative, respectively, than VO_x/SiO_2 (Table 2); both of these contributions cause the $k_2/$ k_1 values to be smaller on MoVTeNbO (Figure 3).

The $\Delta H_3 - \Delta H_1$ and $\Delta S_3 - \Delta S_1$ are more negative than $\Delta H_2 - \Delta H_1'$ and $\Delta S_2 - \Delta S_1'$ on VO_x/SiO_2 , suggesting that transition states for sequential oxygenate formations exhibit enthalpy-entropy tradeoffs analogous to but stronger than the parallel reactions. In contrast, the $\Delta H_3 - \Delta H_1$ values are slightly positive, and $\Delta S_3 - \Delta S_1$ values are near zero on MoVTeNbO, suggesting that, for these oxides, sequential oxygenate formation steps have slightly higher activation enthalpy than the ODH steps but similar entropy losses for both. Such enthalpic favorability of ODH over secondary reactions appears to be unique to the M1 phase among Vcontaining oxides because, on other oxides, selectivity increases with temperature and gives comparable selectivity to the M1 phase (at same conversion) only at much higher temper-

The oxygenate formation reactions require at least one C-O bond formation step, but the nature of intermediates and transition states involved can vary among different catalysts and measured barriers may even include contributions from multiple paths. These different possible pathways are shown in Scheme 2, and their energetics are analyzed next using DFT calculations for C-H activation and C-O bond formation steps for C₂H₆ and C₂H₄ on V₂O₅(001), MoVTeNbO sevenmembered ring pores, and MoVTeNbO(001) models.

3.3. C-H Activation and C-O Formation Pathways on V₂O₅(001) Surfaces. The vdW-DF2-derived electronic

Scheme 2. Reaction Branches for (a) C₂H₆, (b) •C₂H₅, and (c) C₂H₄ Reactants

energies, Gibbs free energies at 648 K and 1 kPa pressure of gaseous reactants, and structures of intermediates and transition states involved in most favorable elementary steps for the formation of C2H4 and oxygenates via primary and secondary reactions of C2H6 on the V2O5(001) surface are shown in Figure 4. The enthalpies, entropies, and free energies for these intermediates and transition states are listed in Table \$5 (Supporting Information).

3.3.1. C_2H_5 Radical Formation from C_2H_6 . The adsorptions of C₂H₆ and C₂H₄ exhibit slightly negative electronic energies that indicate weak vdW interactions of these species with the surface ($\Delta E_{\rm MO~^*-C_2H_6}$ = $-13~{\rm kJ~mol^{-1}}$ and $\hat{\Delta} E_{\rm MO~^*-C_2H_4}$ = -16 kJ mol⁻¹, Figure 4a). These stabilizations are offset by entropy loss resulting from the adsorption of gaseous species on the surface, which leads to positive Gibbs free energies and, in turn, suggests that these molecules do not attain significant surface coverage at reaction conditions ($\Delta G_{\text{MO}} *_{- C_2H_6} = 44 \text{ kJ}$ mol^{-1} and $\Delta G_{\text{MO}} * {}_{-\text{C}_{2}\text{H}_{4}} = 48 \text{ kJ mol}^{-1}$, Figure 4b). C-H activation in adsorbed C₂H₆ forms a surface OH bond at V= O terminal O atom with an unpaired electron at the metal center and $\cdot C_2H_5$ radical interacting with it ($\cdot MOH^* - \cdot C_2H_5$). For the transition state mediating the C-H activation, the electronic energy (ΔE_{TS01}) and Gibbs free energy (ΔG_{TS01}) referenced to gaseous C₂H₆ are 122 and 198 kJ mol⁻¹, respectively.

The $\cdot C_2H_5$ radical formed from C-H activation in C_2H_6 can reverse the first C-H activation to reform C₂H₆ or (i) undergo second C-H activation near the first C-H activation site location, (ii) desorb into the gas phase to carry out the second C-H activation at other catalytic sites, or (iii) undergo C-O bond formation near the C-H activation site or at a different site upon desorption, depending on which of these possibilities exhibit low barriers and abundant reactive sites, and therefore contribute significantly to overall reaction rates. Experimental measurements have shown that the first C-H activation is typically irreversible in Mars-van Krevelen cycles, and yet, second C-H activation at the same location presents a greater barrier than the first one ($\Delta E_{TS 2nd CH} = 144$, Figure S3; $\Delta E_{\text{TS01}} = 122 \text{ kJ mol}^{-1}$, Figure 4a). Previous DFT studies on $V_2O_5(001)$ and V-substituted silsesquioxane clusters representing VO_x/SiO₂ are consistent with higher transition-state energies for second C-H activation at same locations. 31,34 This suggests that desorption-mediated routes or C-O formation routes at the same or different locations must be more prevalent. The electronic energy for desorbed $\cdot C_2H_5$ radical species is higher than that for the radical species on the surface ($\Delta E_{C_2H_5(g)} = 147 \text{ kJ mol}^{-1} \text{ and } \Delta E_{\cdot \text{MOH *} - \cdot \cdot C_2H_5} = 103$ kJ mol⁻¹, Figure 4a), suggesting that the radical exhibits electronic radical-radical interactions with the surface, which is stronger than the weak vdW interactions that stabilize C₂H₆ on the surface $(\Delta E_{C_2H_6(g)} = 0 \text{ kJ mol}^{-1}, \Delta E_{MO} *_{-C_2H_6} = -13 \text{ kJ}$ mol⁻¹). The desorption of the radical also leads to entropy gain for the desorbed molecule, which causes the free energy to be lower and suggests that desorption is highly favored $(\Delta G_{\cdot C_2H_5(g)} = 124 \text{ kJ mol}^{-1}, \Delta G_{\cdot \text{MOH}} *_{-\cdot C_2H_5} = 171 \text{ kJ mol}^{-1}).$ This facile desorption of radicals is consistent with experimental detection of small concentrations of $\cdot C_2H_5$ radicals during C₂H₆ ODH on metal oxides.⁹⁰

3.3.2. C_2H_4 and Oxygenate Formation from the C_2H_5 *Radical.* The rebound reaction of the $\cdot C_2H_5$ radical at $\cdot MOH^*$ to form $MO(H)C_2H_5^*$, a precursor to $C_2H_5OH(g)$, presents

The Journal of Physical Chemistry C

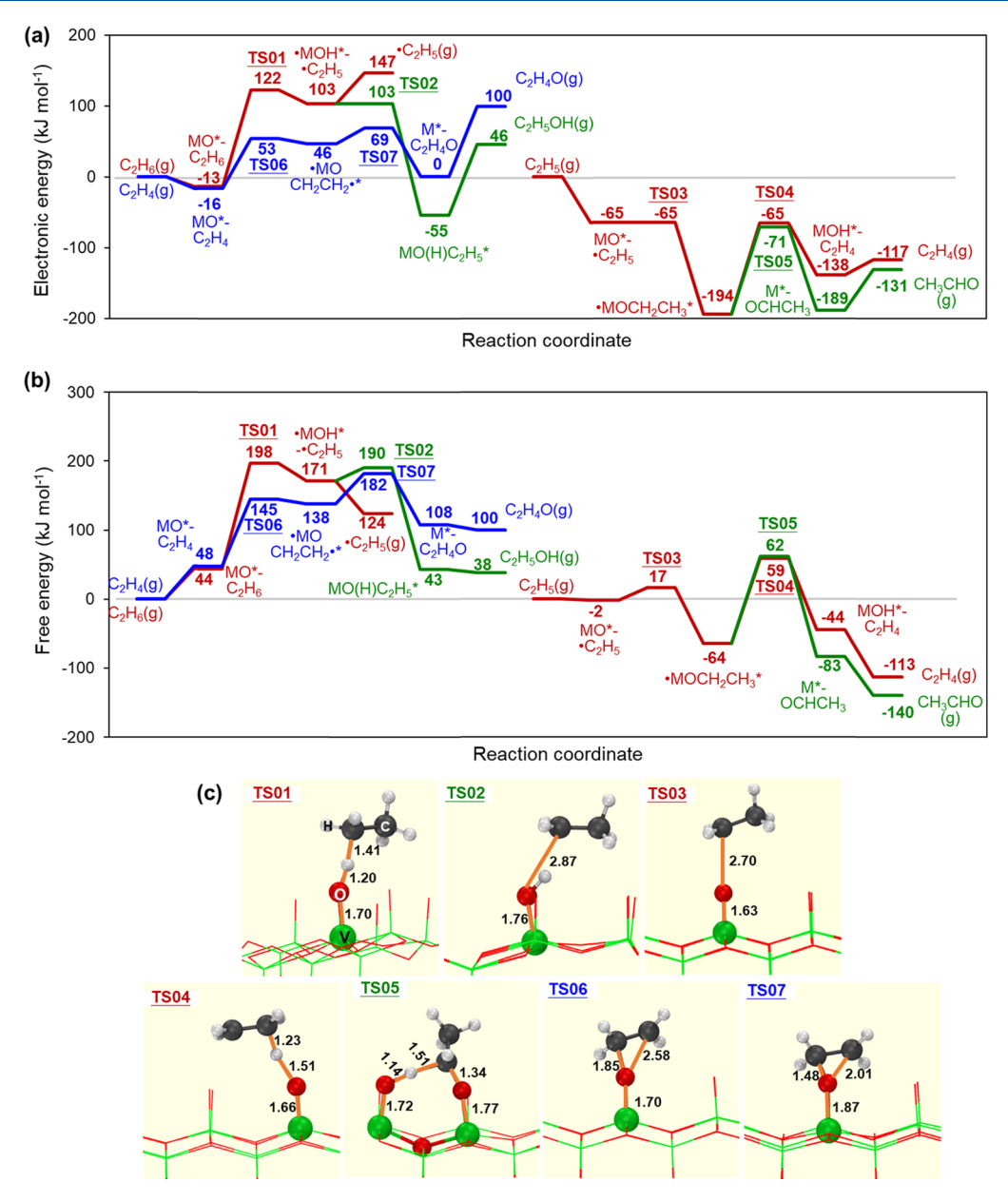


Figure 4. vdW-DF2-derived (a) electronic energies, (b) Gibbs free energies (at 1 kPa and 648 K), and (c) structures of transition states for C–H activation in C_2H_6 and C_2H_5 radicals to form C_2H_4 (red) and C–O bond formations via parallel steps for C_2H_5 radicals (green) and sequential steps for C_2H_4 (blue) at O atoms on the $V_2O_5(001)$ surface.

no electronic energy barrier along the minimum energy path, leading to no formal transition state being found. The highest point along the reaction coordinate for this step is the weakly adsorbed radical (·MOH* $-\cdot$ C₂H₅ species, Figure 4), and the energy monotonically decreases as the reaction proceeds. This rebound step, however, forms a rigid C–O bond, which requires the loss of a degree of freedom along the reaction coordinate for the approaching C atom in the radical toward the O atom. Therefore, the free energy barrier for this step was determined by using the electronic energy of the initial · MOH* $-\cdot$ C₂H₅ species and neglecting a translational degree of freedom that would lie along the reaction coordinate (ΔE_{TSO2} = 103 kJ mol $^{-1}$ and ΔG_{TSO2} = 190 kJ mol $^{-1}$, Figure 4). Such rebound reactions, as well as reversals of first C–H activation, are unlikely to proceed with significant rates because they require surface ·MOH* species that have very low surface coverage due to the reaction of such species with

 O_2 in rapid reoxidation steps in Mars—van Krevelen cycles. ^{33,34} The reoxidations make the MO* species the most abundant surface species, and $\cdot C_2H_5$ radicals can bind and react at such species via steps described next.

The adsorption of the $\cdot C_2H_5(g)$ radical on the surface is significantly strong ($\Delta E_{\text{MO}} *_{-} \cdot C_2H_5 = -65 \text{ kJ mol}^{-1}$, Figure 4). This species forms a C–O bond at terminal MO* (V=O) in highly exothermic steps, leading to an ethoxy species with no electronic energy barrier ($\Delta E_{\cdot \text{MOCH}_2\text{CH}_3^*} = -194 \text{ kJ mol}^{-1}$ and $\Delta G_{\cdot \text{MOCH}_2\text{CH}_3^*} = -64 \text{ kJ mol}^{-1}$, Figure 4). The activation barrier for this step is determined by neglecting the free energy contributions to the translational degree of freedom along the C–O formation coordinate ($\Delta E_{\text{TS03}} = -65 \text{ kJ mol}^{-1}$ and $\Delta G_{\text{TS03}} = 17 \text{ kJ mol}^{-1}$, Figure 4). C–H activation at the CH₃ group in the β position to the C–O bond using a vicinal terminal V=O O atom as the H abstractor leads to the

Table 3. vdW-DF2-Derived Electronic Energies, Enthalpies, Entropies, and Gibbs Free Energies (at 1 kPa and 648 K) for Kinetically Relevant Transition States in C₂H₆ ODH and Parallel and Sequential Oxygenate Formation Paths on V₂O₅(001)

reaction	kinetically relevant TS	$\Delta E_{\mathrm{TS}} \; (\mathrm{kJ} \; \mathrm{mol}^{-1})$	ΔH_{TS} (kJ mol ⁻¹)	$\Delta S_{\mathrm{TS}} \left(\mathrm{J~mol^{-1}~K^{-1}} \right)$	$\Delta G_{ m TS}~({ m kJ~mol}^{-1})$
$C_2H_6 \rightarrow \cdot C_2H_5$	TS01	122	105	-143	198
$\cdot C_2H_5 \rightarrow C_2H_4$	TS04	-65	-68	-197	59
$\cdot C_2H_5 \rightarrow CO_xH_y$	TS05	- 71	-74	-211	62
$C_2H_4 \rightarrow CO_xH_y$	TS07	69	67	-176	182

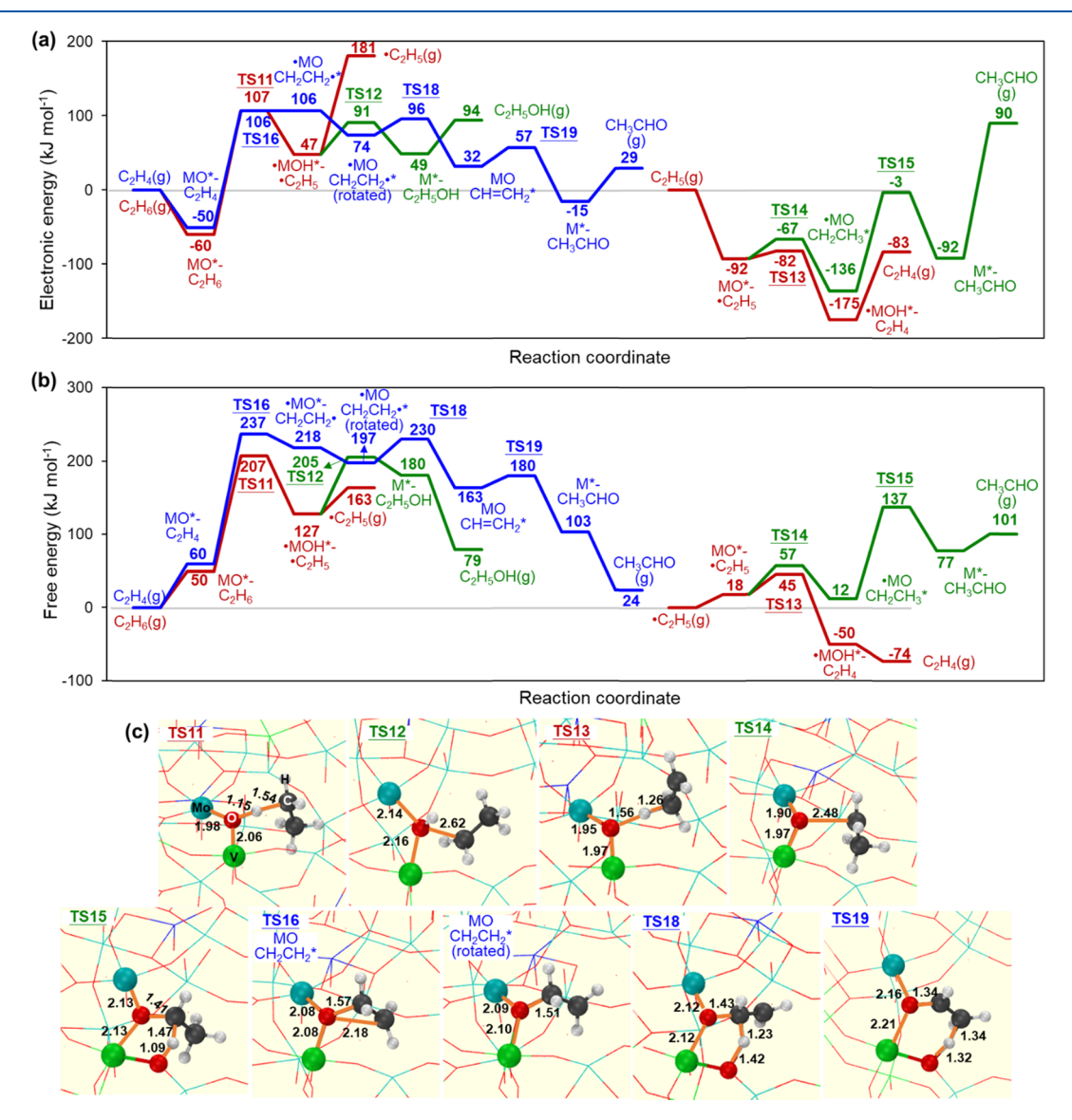


Figure 5. vdW-DF2-derived (a) electronic energies, (b) Gibbs free energies (at 1 kPa and 648 K), and (c) structures of intermediates and transition states for C-H activation in C_2H_6 and C_2H_5 radicals to form C_2H_4 (red) and C-O bond formations via parallel steps for C_2H_5 radicals (green) and sequential steps for C_2H_4 (blue) at O atoms accessible in pores of MoVTeNbO.

formation of C_2H_4 and an OH group ($\Delta E_{TS04} = -65$ kJ mol⁻¹ and $\Delta G_{TS04} = 59$ kJ mol⁻¹, Figure 4). An alternate path involves C–H activation in the CH₂ group in the α position, leading to the formation of an OH group and a MOCHCH₃* species ($\Delta E_{TS05} = -71$ kJ mol⁻¹ and $\Delta G_{TS05} = 62$ kJ mol⁻¹, Figure 4). The MOCHCH₃* species subsequently desorbs to form an O vacancy (M*) and CH₃CHO. Thus, on $V_2O_5(001)$ surfaces, the transition state for the CH₃CHO oxygenate formation step (TS05) exhibits lower activation enthalpy than the C_2H_4 formation step (TS04), suggesting that parallel C–O bond formations have slightly lower activation energy than

ODH, which is consistent with k_2/k_1 values near unity in measurements. CH₃CHO contains weak C–H bonds, making it highly reactive for subsequent reactions, leading to CO and CO₂ via steps that are not examined here but have been shown to be very facile on oxides.^{33,92}

3.3.3. Sequential Reactions of C_2H_4 . C–H activation energies in different molecules at the same lattice O atom depend strongly on C–H bond dissociation energy (BDE). The C_2H_4 molecule consists of much stronger C–H bonds than C_2H_6 (BDE values of 464 and 421 kJ mol⁻¹ in C_2H_4 and C_2H_6 , respectively), and therefore, it exhibits

much higher activation energies for a direct homolytic C-H bond activation at sp2 hybridized carbon. The more facile secondary reaction in C₂H₄ must involve a C-O bond formation. A physisorbed C₂H₄ forms a ·MOCH₂CH₂·* species at the V=O terminal O atom via a C-O bond formation transition state ($\Delta E_{\rm TS06}$ = 53 kJ mol⁻¹ and $\Delta G_{\rm TS06}$ = 145 kJ mol⁻¹, Figure 4). This adsorbed C₂H₄ may desorb or undergo (i) second C-O formation between the same O atom and C atom in the β position, leading to an adsorbed epoxy species (M*-C₂H₄O) or (ii) C-H activation at the CH₂ group in the α position using a vicinal V=O O atom, leading to adsorbed vinyl (MOCH=CH2*) species shown in Scheme 2c. The CH₂ group in MOCH=CH₂* in (ii) can abstract the H atom to form MOCHCH3*, a precursor to CH3CHO. The vdW-DF2-derived energies indicate that the MC₂H₄O* formation path is favorable ($\Delta E_{\rm TS07}$ = 69 kJ mol⁻¹ and $\Delta G_{\rm TS07} = 182 \text{ kJ mol}^{-1}$, Figure 4) over the MOCHCH₃* formation path ($\Delta E_{\rm TS08} = 87 \text{ kJ mol}^{-1}$ and $\Delta G_{\rm TS08} = 201 \text{ kJ}$ mol⁻¹, Figure S4, Supporting Information). Previous studies on V2O5 surfaces using the PBE functional did not consider such epoxidation steps and concluded CH3CHO formations to be the main path for secondary oxidation of C_2H_4 .³³ The desorption of C₂H₄O from adsorbed MC₂H₄O* species leaves an O vacancy with a significant electronic energy penalty $(\Delta E_{\text{MC}_2\text{H}_4\text{O}^*} = 0 \text{ kJ mol}^{-1} \text{ and } \Delta E_{\text{C}_2\text{H}_4\text{O}(g)} = 100 \text{ kJ mol}^{-1},$ Figure 4) but a corresponding entropy gain for the desorbed molecule, which leads to a favorable Gibbs free energy for desorption ($\Delta G_{\text{MC}_2\text{H}_4\text{O}^*} = 108 \text{ kJ mol}^{-1} \text{ and } \Delta G_{\text{C}_2\text{H}_4\text{O}(g)} = 100$ kJ mol⁻¹, Figure 4). The C₂H₄O molecule can isomerize to CH₃CHO on a MO* or MOH* site. 25 CH₃CHO contains much weaker C-H bonds than reactants and undergoes rapid oxidation to CO or CO2, suggesting that these initial C-O bond formation steps limit the sequential oxidation of C₂H₄, which determines the selectivity shown in Figures 2 and 3 and interpreted in the form of rate constant ratios. The Gibbs free energy for epoxidation is lower than that for primary C-H activation in C_2H_6 ($\Delta G_{TS07} = 182 \text{ kJ mol}^{-1}$ and $\Delta G_{TS01} = 198$ kJ mol⁻¹, Figure 4), consistent with k_3/k_1 values much higher than unity in measurements (Figure 3).

The barriers for kinetically relevant steps determined from points with highest Gibbs free energy along reaction coordinates in Figure 4 for C₂H₆ ODH and parallel and sequential conversion to oxygenates on V₂O₅(001) are shown in Table 3. These values represent the overall barriers to the steps in Scheme 1b), which determine the measured rate constant ratios given by eqs 8 and 11. The C-H activation transition states exhibit higher activation enthalpies and lose less entropy than relevant C-O bond formations, which is consistent with measurements (Table 2).

3.4. C—H Activation and C—O Formation Pathways in MoVTeNbO Pores. The vdW-DF2-derived electronic energies, Gibbs free energies at 648 K and 1 kPa pressure of gaseous reactants, and the structures of intermediates and transition states for most favorable steps for the formation of C2H4 and oxygenates via primary and secondary reactions of C₂H₆ (Scheme 2) inside seven-membered ring pores of M1phase MoVTeNbO oxides are shown in Figure 5. The enthalpies, entropies, and free energies for each intermediate and transition state are listed in Table S7 (Supporting Information). The pore environment of bulk MoVTeNbO imposes vdW stabilizations much stronger than (001) surfaces of V₂O₅ due to the proximity to a larger number of lattice

atoms in voids of dimensions similar to the reactive species. These pores also do not contain accessible terminal M=O O atoms, which leads to significant modifications to activation energies and structures of most favored C-O bond formation steps. The most reactive O atom accessible inside the pores determined from HAE calculations is a V-O-Mo bridging O atom (site 4, Figure 1).

3.4.1. C_2H_5 Radical Formation from C_2H_6 . The electronic energies for the adsorption of C₂H₆ and C₂H₄ in MoVTeNbO pores are much more negative than those of the $V_2O_5(001)$ surface because vdW interactions are stronger inside the pores $(\Delta E_{\text{MO} * - C_2H_6} = -60 \text{ kJ mol}^{-1} \text{ and } \Delta E_{\text{MO} * - C_2H_4} = -50 \text{ kJ}$ mol⁻¹, Figure 5). These molecules, however, are confined tightly inside the pores, which leads to loss of translational and rotational degrees of freedom available to loosely physisorbed molecules at outer surfaces and, in turn, causes greater entropy losses and positive adsorption free energies similar to (001) surfaces ($\Delta G_{\rm MO}*_{-{\rm C}_2{\rm H}_6}$ = 50 kJ mol $^{-1}$ and $\Delta G_{\rm MO}*_{-{\rm C}_2{\rm H}_4}$ = 60 kJ mol⁻¹, Figure 5). The influence of stronger vdW stabilization is also important for transition state for C-H activation inside the pores at the V-O-Mo bridging O atom with the most negative HAE (Table 1; site 4, Figure 1). This transition state exhibits lower electronic energy than the V=O terminal O atom in the $V_2O_5(001)$ surface (ΔE_{TS11} = 107 kJ mol^{-1} , Figure 5; $\Delta E_{\text{TS01}} = 122 \text{ kJ mol}^{-1}$, Figure 4), despite a more negative HAE value for the latter O atom (Table 1). A slightly more stable configuration of this transition state was found compared to the values reported previously.⁵⁴ The greater entropy loss inside the pores, however, causes the Gibbs free energies to be higher ($\Delta G_{TS11} = 207 \text{ kJ mol}^{-1}$, Figure 5; $\Delta G_{TS01} = 198 \text{ kJ mol}^{-1}$, Figure 4). The stabilization due to vdW in pores is more significant at lower temperatures because of a smaller free energy penalty from the entropy loss in pores. Desorption of the $\cdot C_2H_5$ radical out of the pores leads to higher free energy than the radical inside the pore $(\Delta G_{C,H_s(g)} = 163 \text{ kJ mol}^{-1}, \Delta G_{\cdot MOH * - \cdot C,H_s} = 127 \text{ kJ mol}^{-1},$ Figure 5) but lower than that of the C–H activation transition state, suggesting that desorption is facile. The ·C₂H₅ radical may undergo second C-H activation to form C2H4 at a different O atom location within the pore or desorb to readsorb at a different pore to complete these steps.

3.4.2. C_2H_4 and Oxygenate Formation from the C_2H_5 *Radical.* The rebound of $\cdot C_2H_5$ radical at minority $\cdot MOH^*$ sites forms MO(H)C₂H₅* species via a C-O bond formation transition state that leads to C₂H₅OH as the desorbed product $(\Delta E_{\rm TS12} = 91 \text{ kJ mol}^{-1}, \Delta G_{\rm TS12} = 205 \text{ kJ mol}^{-1}, \text{ Figure 5}). \text{ This}$ step likely does not contribute significantly to C2H5 radical reactions due to low concentrations of ·MOH* and much higher concentrations of MO* sites that convert •C₂H₅. ^{33,34} The ·C₂H₅ species physisorbs in a pore with much more negative electronic energy than the V₂O₅(001) surface $(\Delta E_{\cdot MO} * - \cdot C_{\cdot H_s} = -92 \text{ kJ mol}^{-1}, \text{ Figure 5}). \text{ Direct C-H}$ activation of a second C-H bond from the physisorbed radical to form C₂H₄ presents a lower barrier than the ethoxy formation step because C-O bond formations are hindered in the pores with highly restricted access to terminal O atoms and steric hindrance to C-O bonds in concave pores with bridging O atoms ($\Delta E_{TS13} = -82 \text{ kJ mol}^{-1}$, $\Delta G_{TS13} = 45 \text{ kJ mol}^{-1}$; $\Delta E_{\rm TS14} = -67 \text{ kJ mol}^{-1} \text{ and } \Delta G_{\rm TS14} = 57 \text{ kJ mol}^{-1}$, Figure 5). Second C-H activation at the α CH₂ group in ethoxy species leads to the formation of MOCHCH3* that desorbs as

Table 4. vdW-DF2-Derived Electronic Energies, Enthalpies, Entropies, and Gibbs Free Energies (at 1 kPa and 648 K) for Kinetically Relevant Transition States in C_2H_6 ODH and Parallel and Sequential Oxygenate Formation Paths inside MoVTeNbO Pores

reaction	kinetically relevant TS	$\Delta E_{\rm TS}$ (kJ mol ⁻¹)	$\Delta H_{\rm TS}$ (kJ mol ⁻¹)	ΔS_{TS} (J mol ⁻¹ K ⁻¹)	$\Delta G_{ m TS}$ (kJ mol ⁻¹)
$C_2H_6 \rightarrow \cdot C_2H_5$	TS11	107	94	-173	207
$\cdot C_2H_5 \rightarrow C_2H_4$	TS13	-82	-84	-199	45
$\cdot C_2H_5 \rightarrow CO_xH_y$	TS15	-3	-4	-218	137
$C_2H_4 \rightarrow CO_xH_y$	TS16	106	109	-198	237

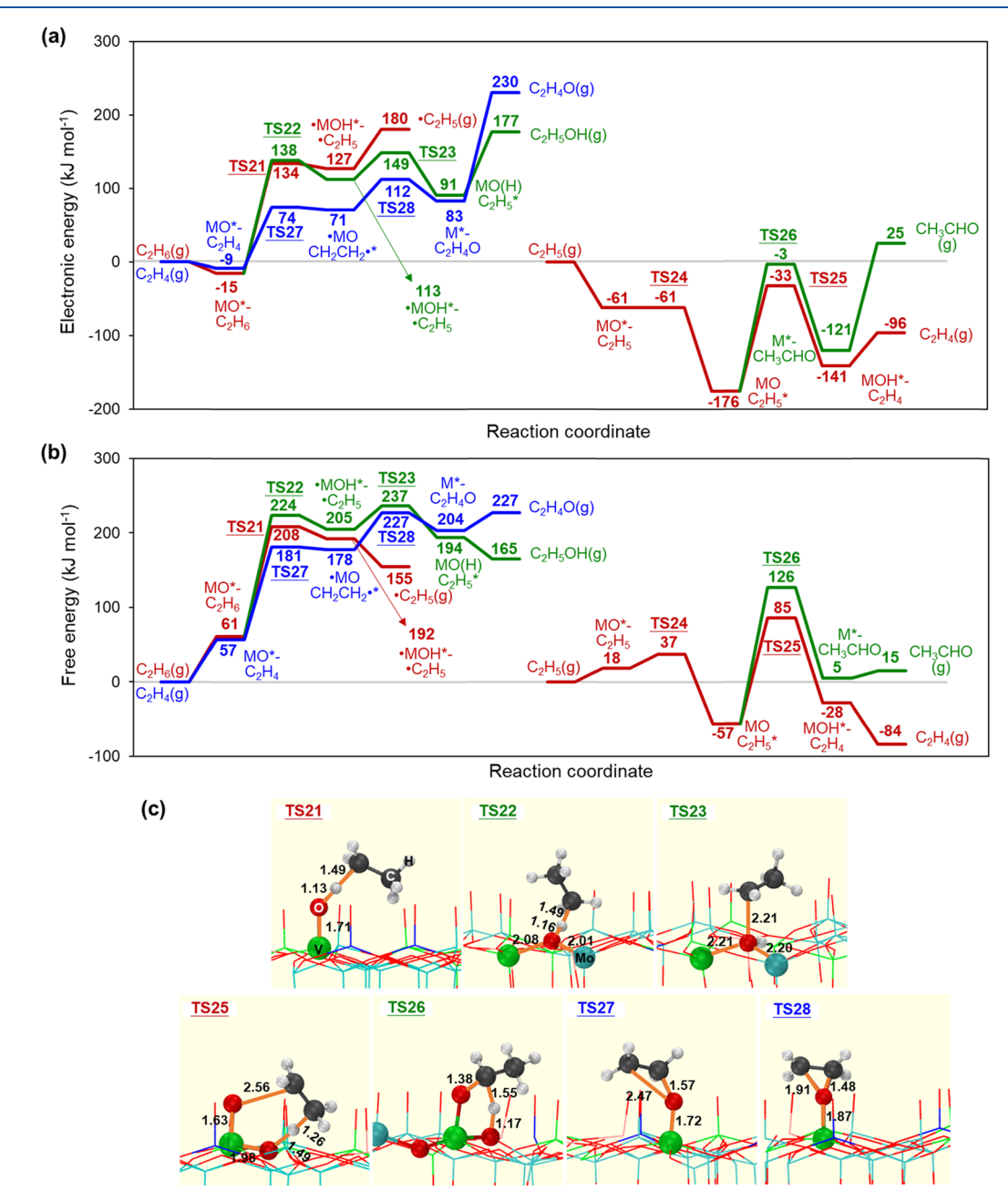


Figure 6. vdW-DF2-derived (a) electronic energies, (b) Gibbs free energies (at 1 kPa and 648 K), and (c) structures of intermediates and transition states for C-H activation in C_2H_6 and C_2H_5 radicals to form C_2H_4 (red) and C-O bond formations via parallel steps for C_2H_5 radicals (green) and sequential steps for C_2H_4 (blue) at O atoms from the (001) surface of MoVTeNbO.

CH₃CHO ($\Delta E_{TS15} = -3 \text{ kJ mol}^{-1} \text{ and } \Delta G_{TS15} = 137 \text{ kJ mol}^{-1}$, Figure 5).

3.4.3. Sequential Reactions of C_2H_4 . Despite stronger vdW stabilizations in the pores, the C_2H_4 adsorption via C–O bond formation at the V–O–Mo bridging O atom location (site 4,

Figure 1) within MoVTeNbO pores is much more endothermic than at the terminal O atom on $V_2O_5(001)$ surfaces ($\Delta E_{\cdot MOCH_2CH_2}$.* = 46 and 106 kJ mol⁻¹ in Figures 4 and 5, respectively). Such adsorption at the terminal O atom from within the pores is even more endothermic because

access to terminal O atoms between layers is strongly hindered inside the pores (132 kJ mol⁻¹ for site 5, Table S8, Supporting Information). These differences from the nonconfining (001) surfaces contribute significantly to the high selectivity in M1phase catalysts. The formation of the C-O bond at the bridging location from physisorbed C2H4 occurs without a formal transition state because the energy increases monotonically as the adsorption proceeds, as in the case of MO(H)- $C_2H_5^*$ formation on $V_2O_5(001)$. The barriers are therefore calculated based on electronic energy of the product state and removal of one translational degree of freedom for the approach of the molecule to the surface along the reaction coordinate. The second C-O bond formation in · MOCH₂CH₂·* leading to M*-C₂H₄O epoxide species exhibits large barriers due to steric hindrance in bridging O atoms and the concave pore structure ($\Delta E_{TS17} = 147 \text{ kJ mol}^{-1}$ and $\Delta G_{TS17} = 283 \text{ kJ mol}^{-1}$, Figure S5). Instead, · MOCH₂CH₂·* species undergo a more facile C-H activation in the CH_2 group at the α position to form MOCH= CH_2 * species. This C-H activation first requires a 90° rotation of the CH_2 group in the β position that changes the hybridization of the α C atom to decrease the C-H bond energy for a facile C-H activation. This rotation is barrierless, and subsequent C-H activation transition state leads to MOCH=CH₂* $(\Delta E_{\rm TS18} = 96 \text{ kJ mol}^{-1} \text{ and } \Delta G_{\rm TS18} = 230 \text{ kJ mol}^{-1}, \text{ Figure 5}).$ This species then forms a C–H bond in the β position to form MOCHCH₃* species ($\Delta E_{TS19} = 57 \text{ kJ mol}^{-1}$ and $\Delta G_{TS19} = 180$ kJ mol⁻¹, Figure 5), which desorbs as CH₃CHO ($\Delta E_{\text{CH}_3\text{CHO}(g)}$ = 29 kJ mol⁻¹ and $\Delta G_{\text{CH}_3\text{CHO}(g)}$ = 24 kJ mol⁻¹, Figure 5) in kinetically irrelevant steps. The CH3CHO molecules can undergo subsequent fast oxidation to form CO and CO2. For the C₂H₄ oxidation reaction, the initial C-O bond formation for C2H4 adsorption presents the highest barrier along the reaction coordinate.

The barriers for kinetically relevant steps determined from points with the highest Gibbs free energy along reaction coordinates in Figure 5 for C₂H₆ ODH and parallel and sequential conversion to oxygenates inside MoVTeNbO pores are shown in Table 4. For these pore environments, transition states for C-H activation steps exhibit lower enthalpy than relevant C-O bond formation steps, which contrasts V₂O₅(001) and shows much higher C₂H₄ selectivity. The entropy loss for C-H activation steps is also lower than C-O bond formation. Therefore, the pores favor C-H activations via enthalpic as well as entropic effects and will remain selective to C₂H₄ at both low and high temperatures (eqs 8 and 11; Scheme 1b and Tables 3 and 4).

3.5. C-H Activation and C-O Formation Pathways on the M1 Phase of the MoVTeNbO(001) Surface. The vdW-DF2-derived electronic energies, Gibbs free energies at 648 K and 1 kPa pressure of gaseous reactants, and the structures of intermediates and transition states for most favored paths for the formation of C2H4 and oxygenates via primary and sequential reactions of C₂H₆ (Scheme 2) on the M1 phase of the MoVTeNbO(001) surface are shown in Figure 6. The enthalpies, entropies, and free energies for these intermediates and transition states are listed in Table S9 (Supporting Information). The reactions on MoVTeNbO(001) proceed via elementary steps analogous to V₂O₅(001) but differ in types of O atoms involved and in differences between C-H activation and C-O formation energies. The steps that involved nearest-neighbor V=O pairs

on $V_2O_5(001)$ use a terminal V=O O atom and a bridging O atom on MoVTeNbO(001) due to larger separation between terminal atoms. The V=O sites on MoVTeNbO(001) have been suggested as reactive sites for C-H activation, while their selectivity to C₂H₆ ODH has not been probed. ^{94,95}

3.5.1. C_2H_5 Radical Formation from C_2H_6 . The adsorptions of C₂H₆ and C₂H₄ on MoVTeNbO(001) experience weak vdW stabilizations ($\Delta E_{\text{MO}} * - C_{2}H_{6} = -15 \text{ kJ mol}^{-1}$ and $\Delta E_{\mathrm{MO} * - C_{2}H_{4}} = -9 \text{ kJ mol}^{-1}$) and compensations from entropy losses, leading to free energies similar to $V_2O_5(001)$ $(\Delta G_{\text{MO}} *_{-\text{C},\text{H}_4} = 61 \text{ kJ mol}^{-1} \text{ and } \Delta G_{\text{MO}} *_{-\text{C},\text{H}_4} = 57 \text{ kJ mol}^{-1},$ Figure 6). A transition state for C-H activation in C₂H₆ at V=O terminal O atom (site 5, Figure 1) mediates the formation of ·MOH*-·C₂H₅ species ($\Delta E_{TS21} = 134 \text{ kJ mol}^{-1}$ and $\Delta G_{TS21} = 208 \text{ kJ mol}^{-1}$, Figure 6), with activation energy larger than $V_2O_5(001)$, which is consistent with the less negative HAE on MoVTeNbO (Table 1). The HAE on MoVTeNbO(001) is more negative at the bridging O atom (-269 kJ mol⁻¹ at site 4, Figure 1; Table 1) than the terminal O atom (-254 kJ mol⁻¹ at site 4, Figure 1; Table 1). Yet, the electronic energy for C-H activation in C₂H₆ is slightly more favored at the terminal O atom ($\Delta E_{\text{TS21}} = 134 \text{ kJ mol}^{-1}$, Figure 6; $\Delta E_{\text{TS22}} = 138 \text{ kJ mol}^{-1}$, Table S9, Supporting Information), possibly due to stronger radical-surface interactions between · C₂H₅ and the terminal O atom than the bridging O atom. ²¹ The one-layer MoVTeNbO(001) models lack a subsurface O atom underneath the V=O bond, which prevents delocalization of the unpaired electron in the ·MOH* species formed as the product of the C-H activation. The lower stability of localized electrons leads to less negative HAE at terminal O atoms, but such effects can be compensated by larger interactions between unpaired electrons in ·MOH* and · C₂H₅ pairs in the product, which, in turn, can lead to C-H activation energies lower than the value suggested by HAE. Such effects were previously observed for radicals with different extents of delocalization in unpaired electrons for secondary radical in propane and allylic radical in propene.²¹

The electronic energy for C-H activation at the V-O-Mo bridging O atom in MoVTeNb(001) is 31 kJ mol⁻¹ higher than at the identical location on MoVTeNbO pores (ΔE_{TS11} = 107 kJ mol⁻¹ Figure 5), despite less negative HAE in the latter model, because vdW stabilizations are much stronger inside the pores. The transition state inside the pores, however, loses more entropy, which suggests that C2H6 activates predominantly inside the pores of MoVTeNbO at low and moderate temperatures even when active sites in (001) surfaces are similarly abundant as intrapore sites. The prediction for the effect of temperature of transition from favorability of C-H activation in pores to that in surfaces may depend strongly on small inaccuracies in entropy estimates, which are difficult to obtain precisely when steps involve low-frequency vibrational modes. The estimated Gibbs free energies for activation at surfaces at 648 K are similar to the pores (ΔG_{TS21} = 208 kJ mol^{-1} , Figure 6; $\Delta G_{\text{TS11}} = 207 \text{ kJ mol}^{-1}$, Figure 5), but intrapore sites may be more abundant than surfaces in catalyst samples. The measured rate ratios, however, confirm that C-H activations predominantly occur in pores at 648 K.54 Desorption of the ·C₂H₅ radical to the gas phase is facile because of entropy gain in $\cdot C_2H_5(g)$ ($\Delta G_{\cdot C_2H_5(g)} = 155$ kJ mol^{-1} and $\Delta G_{\cdot \text{MOH} * - \cdot C_2 H_5} = 192 \text{ kJ mol}^{-1}$, Figure 6).

Table 5. vdW-DF2-Derived Electronic Energies, Enthalpies, Entropies, and Gibbs Free Energies (at 1 kPa and 648 K) for Kinetically Relevant Transition States in C₂H₆ ODH and Parallel and Sequential Oxygenate Formation Paths on MoVTeNbO(001)

reaction	kinetically relevant TS	$\Delta E_{\rm TS}~({\rm kJ~mol^{-1}})$	ΔH_{TS} (kJ mol ⁻¹)	ΔS_{TS} (J mol ⁻¹ K ⁻¹)	ΔG_{TS} (kJ mol ⁻¹)
$C_2H_6 \rightarrow \cdot C_2H_5$	TS21	134 (120) ^a	116 (102) ^a	-143	208 (194) ^a
$\cdot C_2H_5 \rightarrow C_2H_4$	TS25	$-33 (-44)^a$	$-37 (-48)^a$	-189	85 (75) ^a
$\cdot C_2H_5 \rightarrow CO_xH_y$	TS26	$-3(-38)^a$	$-8 (-43)^a$	-207	$126 (91)^a$
$C_2H_4 \rightarrow CO_xH_y$	TS28	112 (68) ^a	112 $(67)^a$	-179	$227 (183)^a$

^aValues in parenthesis are derived from electronic energies in Table 6 for two-layer MoVTeNbO(001) models.

3.5.2. C_2H_4 and Oxygenate Formation from the C_2H_5 Radical. C_2H_5OH formation via rebound of the $\cdot C_2H_5$ radical to reduced ·MOH* sites exhibits low electronic energy barriers $(\Delta E_{\rm TS23} = 149 \text{ kJ mol}^{-1}, \text{ Figure 6})$ but is unlikely to contribute to rates because concentrations of ·MOH* species are small due to fast reoxidations. The C2H5 radical adsorbs near MO* sites in MoVTeNbO(001) with adsorption energies similar to $V_2O_5(001) (\Delta E_{MO*-.C_2H_5} = -65 \text{ and } -61 \text{ kJ mol}^{-1} \text{ in Figures}$ 4 and 6, respectively). The adsorbed radical forms an ethoxy species at the terminal O atom (site 5, Figure 1; $\Delta E_{\text{-MOC,H}_s}$ * = -176 kJ mol⁻¹, Figure 6), which undergoes C-H activation at a C-H bond in the β position to the C-O bond using the vicinal M-O-V bridging O atom (site 4, Figure 1) to form C_2H_4 ($\Delta E_{TS25} = -33 \text{ kJ mol}^{-1}$ and $\Delta G_{TS25} = 85 \text{ kJ mol}^{-1}$, Figure 6). The ·MOC₂H₅* species can also undergo C-H activation at the CH₂ group in the α position using site 4 to form MOCHCH₃* ($\Delta E_{TS26} = -3 \text{ kJ mol}^{-1}$ and $\Delta G_{TS26} = 126$ kJ mol $^{-1}$, Figure 6), which desorbs as CH₃CHO(g).

3.5.3. Sequential Reactions of C_2H_4 . The adsorption of C_2H_4 via a C-O bond formation at the terminal O atom of MoVTeNbO(001) exhibits 25 kJ mol⁻¹ higher electronic energy than $V_2O_5(001)$ ($\Delta E_{.MOCH_2CH_2...*} = 46$ and 71 kJ mol⁻¹ in Figures 4 and 6, respectively). The electronic energy of adsorption at the Mo-O-V bridging O atom of MoVTeNbO is higher by 74 kJ mol⁻¹ than the terminal O atom adsorption on V_2O_5 ($\Delta E_{.MOCH_2CH_2...*} = 120$ kJ mol⁻¹, Figure S6), which suggests that bridging O atoms hinder C-O bond formation. This bridge site adsorption energy on MoVTeNbO(001) surface is +14 kJ mol⁻¹ higher than adsorption at an identical site within the MoVTeNbO pore ($\Delta E_{.MOCH_2CH_2...*} = 106$ kJ mol⁻¹, Figure 5), which reflects significant vdW stabilization in the pore as well as the partial compensation of this stabilization potentially by more steric hindrances in the pores.

The ·MOCH₂CH₂·* species at a terminal O atom forms a second C-O bond via a transition state that leads to epoxide $(\Delta E_{TS28} = 112 \text{ kJ mol}^{-1} \text{ and } \Delta G_{TS28} = 227 \text{ kJ mol}^{-1}, \text{ Figure 6}).$ The desorption of epoxide leaving a terminal O vacancy is highly endothermic, but the entropy gain from the desorbed product leads to free energies similar to C-O bond formation transition state. Such highly endothermic desorption steps can be assisted by simultaneous O2 adsorption at O vacancy and therefore cannot impose kinetic limitations.²⁸ They also represent the unstable nature of O vacancies in one-layer models that do not contain subsurface O atoms to stabilize the reduced centers, as discussed in Section 3.5.4. Alternative C₂H₄ oxidation paths involving CH3CHO formation occur most favorably at bridging O atoms and lead to energy barriers much higher than epoxidation, as shown in the Supporting Information ($\Delta E_{TS30} = 143 \text{ kJ mol}^{-1} \text{ and } \Delta G_{TS30} = 268 \text{ kJ}$ mol⁻¹, Figure S6). The bridging O atoms involved in these

steps provide the most favorable lattice distances for C–H activation from \cdot MOCH₂CH₂·* species in MoVTeNbO oxide, but the overall activation barrier is higher because of the less stable nature of \cdot MOCH₂CH₂·* formed at this location. Here, epoxidation is more strongly favored over CH₃CHO formation than V₂O₅(001) surfaces, where epoxide formation from C₂H₄ is only slightly more favored over CH₃CHO formation using V=O pairs, and MoVTeNbO pores, where CH₃CHO is strongly favored.

The energies of kinetically relevant transition states relative to gas-phase reactants determined from points with highest Gibbs free energy along reaction coordinates in Figure 6 are shown in Table 5. These values represent the overall barriers for steps relevant to selectivity in Scheme 1b and eqs 8 and 11. These one-layer MoVTeNbO surfaces exhibit transition-state enthalpies for oxygenate formation from C₂H₅ radicals (-8 kJ mol⁻¹, Table 5) less negative than C₂H₄ formation (-37 kJ mol^{-1}). The enthalpy for oxygenate formation from C_2H_4 is also only slightly lower (112 kJ mol⁻¹, Table 5) than primary C-H activation (116 kJ mol-1). Thus, these surfaces exhibit values of $\Delta H_2 - \Delta H_1'$ (29 kJ mol⁻¹), $\Delta H_3 - \Delta H_1$ (-4 kJ mol^{-1}) that are in between the values for $V_2O_5(001)$ and MoVTeNbO pores, suggesting that these oxides are less selective to C2H4 than pores but much more selective than V₂O₅(001) surfaces. The higher selectivity of MoVTeNbO(001) surfaces, however, arises from the lack of subsurface layers in one-layer models, instead of an intrinsic property of the surfaces in the M1 phase, which is probed next using a twolayer model.

3.5.4. Effects of Adding a Second Layer to MoVTeNbO(001) Models. The two-layer MoVTeNb(001) models require a large 21.37 × 26.94 × 19.06 ų supercell with 56 Mo, 16 V, 8 Te, 8 Nb, and 232 O atoms (Figure S2, Supporting Information), which prohibits probing of all plausible reaction paths. Here, we recalculate the electronic energies for some intermediates and for kinetically relevant transition states found using the one-layer model for (i) primary C-H activation in C_2H_6 and epoxidation in C_2H_4 , relevant to $\Delta H_3 - \Delta H_1$ and k_3/k_1 values, and (ii) C-H activation and the C-O bond formation steps in the C_2H_5 radical, relevant to $\Delta H_2 - \Delta H_1'$ and k_2/k_1 values. The energies for these species and comparisons with one-layer models and two-layer $V_2O_5(001)$ models are shown in Table 6.

The HAE at site 5 (terminal O atom, Figure 1) in the two-layer model is more negative (-283 kJ mol^{-1} , Table 6) than the one-layer mode (-256 kJ mol^{-1} , Table 6), indicating that the reactivity of O atoms at the (001) is underestimated without the sublayer. The electronic energies of the transition state for C–H activation in C_2H_6 and its product $\cdot C_2H_5$ radical, referenced to gas-phase C_2H_6 , are 14 and 13 kJ mol⁻¹ lower than values in the one-layer model (Table 6). The transition state energy for C–H activation in a C_2H_5 radical for

Table 6. DFT-Derived H Atom Addition Energy and Electronic Energies of Intermediates and Transition States Involved in C-H Activation and C-O Bond Formation at Terminal O Atoms in One- and Two-Layer Models of MoVTeNbO(001) (Site 5) and in $V_2O_5(001)$ (Site 1)

intermediate or transition state	one-layer slab MoVTeNbO(001)	two-layer slab MoVTeNbO(001)	two-layer slab $V_2O_5(001)$			
MOH*	-256	-283	-286			
	$C_2H_6 \rightarrow$	$\cdot C_2H_5$				
$MO*-C_2H_6$	-15	-17	-13			
TS21	134	120	122			
\cdot MOH* $-\cdot$ C ₂ H ₅	127	114	103			
	$\cdot C_2H_5 \rightarrow$	C_2H_4				
TS25	-33	-44	-65			
	$\cdot C_2H_5 \rightarrow$	CO_xH_y				
TS26	-3	-38	-71			
$C_2H_4 \rightarrow CO_xH_y$						
\cdot MOCH ₂ CH ₂ ·*	74	61	46			
TS28	112	68	69			
$M^* - C_2 H_4 O$	83	12	0			

the two-layer model is also more stable than the one-layer model by 11 kJ mol⁻¹ (TS25, Table 6).

The effect of adding a second layer for steps forming an oxygenated molecule is much stronger than C-H activation steps because these steps require a greater number of electron transfers from molecules to surfaces. The electronic energy for the kinetically relevant transition state in CH3CHO formation form C₂H₅ in the two-layer model is more stable than the onelayer model by 35 kJ mol⁻¹. The electronic energies for Obound C₂H₄ species, transition state for epoxidation, and the product M*-C₂H₄O species for two-layer models are 13, 44, and 71 more stable than the one-layer model. These values suggest that species with a greater degree of O atom transfer to C₂H₄ exhibit greater benefit from the presence of the subsurface layer.

The effects of adding the second layer is consistent with the structural changes observed in MoVTeNbO(001) and V₂O₅(001) slabs with the C-O bond formation steps, which are shown in Figure S7 (Supporting Information). During the epoxidation step, as the C-O bonding becomes stronger, the V=O bonding becomes weaker and the V-O bond elongates. The two-layer slabs are able to compensate for such elongations by achieving a shorter bond distance with the subsurface O atom from the second layer, leading to a delocalization of the electron density for the reduced center at the V atom. Such subsurface layers are absent in the one-layer MoVTeNbO(001) model, which makes the C-O bond formation unfavorable due to greater instability of the V atom losing the O atom. C-H activation steps experience much weaker structural changes than C-O bond formations and, therefore, are stabilized to a much lesser extent by the presence of the second layer. The disparate effects of the subsurface layer for C-H activation and C-O bond formation effects are also reflected in the spin density maps for C-H activation and epoxidation on V₂O₅(001) and MoVTeNb pores shown in Figures S12 and S13 (Supporting Information). C-H activation causes one-electron reduction of the surface, which leads to spin density only in the surface V atom of V₂O₅, while epoxidation with two-electron reduction shows significant spin density in the subsurface layer, suggesting that

electron delocalization to the subsurface is significantly more important for stabilizing C-O bond formation.

The reaction barriers for MoVTeNbO(001) (Table 5) were corrected using electronic energies derived from the two-layer model (Table 6), which leads to differences between C-H activation and C-O formation barriers that are more significantly different from MoVTeNbO pores (Table 4) and similar to the activation energy differences on V₂O₅(001) (Table 3). These values suggest that both MoVTeNbO(001) and V₂O₅(001) surfaces favor parallel oxygenate formations and secondary reactions of C₂H₄ over the C-H activation steps, which leads to low C2H4 selectivity. These corrections are shown by numbers in parentheses for the overall barriers for MoVTeNbO(001) in Table 5. In contrast, the pores of MoVTeNbO are highly selective to C2H4, as shown by activation barriers in Table 4.

The analyses of elementary steps show that first C-H activations irreversibly form ·C₂H₅ radicals that can desorb and diffuse to other O atom site for further reactions. Second C-H activation at the CH_3 group of $\cdot C_2H_5$ radicals, mediated by an ethoxy intermediate in some cases, produces C_2H_4 . The $\cdot C_2H_5$ radicals can also undergo C-O formation to form ethoxy and subsequent C-H activation at the CH₂ group leading to a parallel oxygenate, CH₃CHO. Sequential oxygenates from C₂H₄ are completed by two C-O bond formations leading to C₂H₄O or one C-O bond formation and H atom migration leading to CH₃CHO. At (001) surfaces, C-O bond formations involved in ethoxy and epoxy formations favorably occur on terminal O atoms. Epoxy formation is the favorable sequential oxidation path on V₂O₅(001) and MoVTeNbO(001), while CH₃CHO formation path is favored in pores because of inaccessible terminal V=O sites and different bonding properties and the steric structure of bridging V-O-Mo sites. The barriers for these steps for the three catalyst models are shown in Tables 3-5 along with the corrections to the barriers in MoVTeNbO(001) derived using the two-layer models. The influence of these barriers on rate constant ratios and their comparisons to the measured rate constant ratios are discussed next.

3.6. Activation Enthalpy and Entropy Differences and Rate Constant Ratios Relevant to Selectivity. Table 7 shows vdW-DF2-derived enthalpy and entropy differences between parallel steps involving C-H activation and C-O bond formation in the C_2H_5 radical $(\Delta H_2 - \Delta H_1', \Delta S_2 - \Delta S_1';$ Scheme 1b; eq 8) and between primary C-H activation in C_2H_6 and sequential C_2H_4 oxidation $(\Delta H_3 - \Delta H_1, \Delta S_3 -$

Table 7. vdW-DF2-Derived Enthalpy and Entropy Differences between C-H Activation and C-O Bond Formation in the C_2H_5 Radical via Parallel Steps (ΔH_2 – $\Delta H_1'$, $\Delta S_2 - \Delta S_1'$) and between Primary C-H Activation in C_2H_6 and Sequential C_2H_4 Oxidation $(\Delta H_3 - \Delta H_1, \Delta S_3 \Delta S_1$) on V_2O_5 and MoVTeNbO

	$\Delta \Delta H$ (k	J mol ⁻¹)	$\Delta\Delta S$ (J mol ⁻¹ K ⁻¹)	
model	$\Delta H_2 - \Delta H_1'$	$\Delta H_3 - \Delta H_1$	$\Delta S_2 - \Delta S_1'$	$\Delta S_3 - \Delta S_1$
V ₂ O ₅ (001)	-6	-37	-13	-33
MoVTeNbO pores	+80	+14	-19	-25
MoVTeNbO(001)	$+29 (+4)^a$	$-4(-35)^a$	-18	-36

^aValues in parentheses include corrections to electronic energies derived from adding a second layer to the MoVTeNb(001) model.

The Journal of Physical Chemistry C

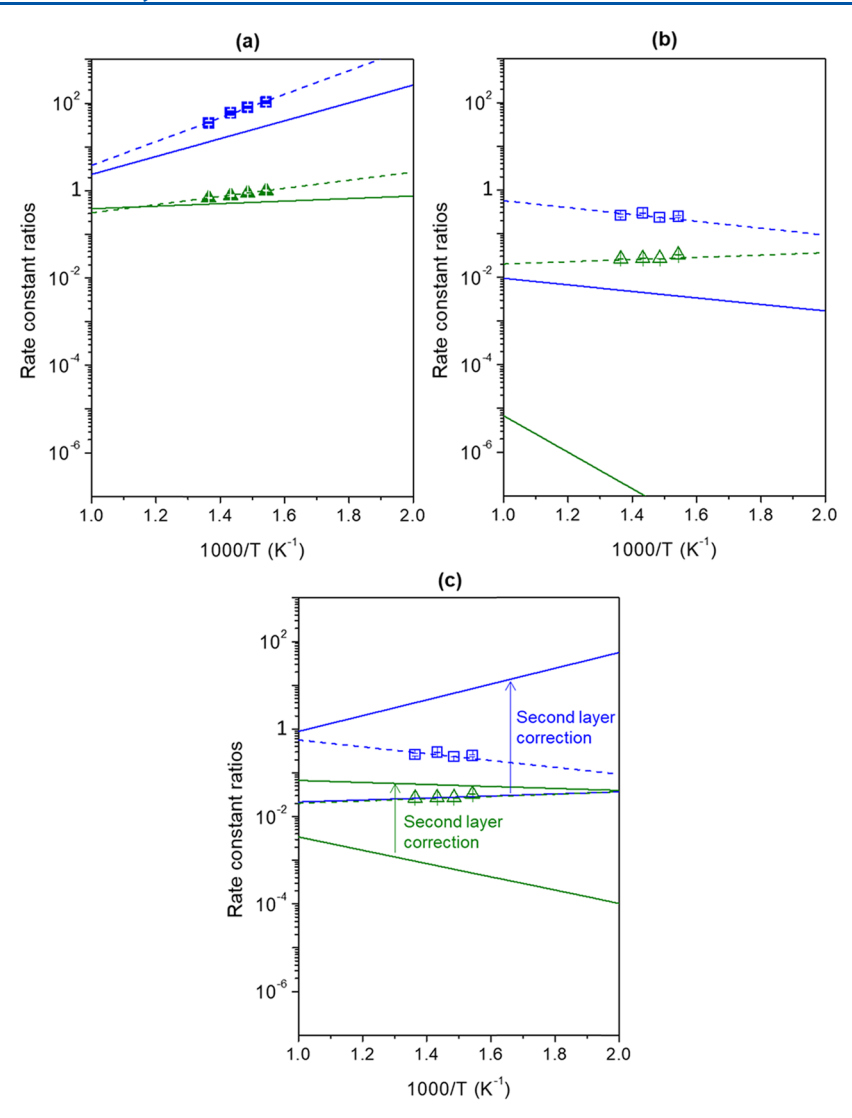


Figure 7. vdW-DF2-derived and measured rate constant ratios k_2/k_1 (green lines, triangle symbols) and k_3/k_1 (blue lines, square symbols) relevant to C_2H_4 selectivity in C_2H_6 ODH as a function of reciprocal temperature on (a) the $V_2O_5(001)$ model and VO_x/SiO_2 catalyst, (b) the MoVTeNbO bulk pore model and MoVTeNbO catalyst, and (c) the MoVTeNbO(001) model and MoVTeNbO catalyst. Dashed lines represent best regression fits to the forms of eqs 8 and 11. Solid lines represent predicted trends form Table 7 and eqs 8 and 11.

 ΔS_1 ; Scheme 1b; eq 8) on $V_2O_5(001)$ and MoVTeNbO pores and MoVTeNbO(001). These values are derived from differences among activation barriers in Tables 3–5 for each catalyst model, and they determine rate constant ratios relevant to C_2H_4 selectivity, as described by Scheme 1a and eqs 8 and 11. The corresponding measured enthalpy and entropy differences derived from measured rate constant ratios on VO_x/SiO_2 and MoVTeNbO samples are shown in Table 2. The measured and DFT-derived rate constant ratios are compared in Figure 7.

The vdW-DF2-derived $\Delta H_2 - \Delta H_1'$ and $\Delta S_2 - \Delta S_1'$ values on $V_2O_5(001)$ (-6 kJ mol⁻¹ and -13 J mol⁻¹ K⁻¹, respectively, Table 7) and the corresponding measured values on VO_x/SiO_2 (-18 ± 1 kJ mol⁻¹ and -28 ± 1 J mol⁻¹ K⁻¹, respectively, Table 2) exhibit negative values, which show that enthalpies favor oxygenate formation steps, while entropy losses favor C_2H_4 formation. The enthalpy—entropy trade-offs for DFT-derived values are slightly weaker than the measurements, leading to rate constants of similar magnitudes but lower temperature dependence in DFT values $(k_2/k_1$, Figure 7a). The DFT-derived $\Delta H_3 - \Delta H_1$ and $\Delta S_3 - \Delta S_1$ values

 $(-37 \text{ kJ mol}^{-1} \text{ and } -33 \text{ J mol}^{-1} \text{ K}^{-1}, \text{ Table } 7)$ are very similar to the corresponding measured values $(-44 \pm 4 \text{ kJ mol}^{-1} \text{ and})$ -34 ± 6 J mol⁻¹ K⁻¹, Table 2), which leads to k_3/k_1 values only slightly lower than measurements (Figure 7a). Small differences between computation and measurements may arise from a variety of factors including the requirement of more than two layers to accurately describe V₂O₅ surfaces, inaccuracies in low-frequency and harmonic oscillator estimates or in DFT functionals, and requirements for ensemble averaging over multiple configurations or steps for reactions. They are unlikely to arise, however, from O vacancies because reoxidation of reduced centers in these samples is rapid⁵⁴ or from peroxo species because reoxidation steps tend to favor "outer-sphere" routes over those that form peroxo species by making and breaking M-O bonds in the "inner sphere".²²

Reactions inside the MoVTeNbO pores lead to DFT-derived $\Delta H_2 - \Delta H_1'$ values that are much higher than measurements on MoVTeNbO catalyst samples (-5 \pm 7 and +80 kJ mol⁻¹ in Tables 2 and 7, respectively) and DFT-derived $\Delta S_2 - \Delta S_1'$ values less negative than measurements (-37 \pm 11

and -19 J mol⁻¹ K⁻¹ in Tables 2 and 7, respectively). The $\Delta H_3 - \Delta H_1$ values from DFT are similar to measured values $(+15 \pm 10 \text{ and } +14 \text{ kJ mol}^{-1} \text{ in Tables 2 and 7, respectively}),$ but the $\Delta S_3 - \Delta S_1$ values are more negative than measurements $(+10^{\circ} \pm 15^{\circ} \text{ and } -25^{\circ} \text{ J mol}^{-1} \text{ K}^{-1} \text{ in Tables 2 and 7,}$ respectively). The k_2/k_1 values derived from DFT are 3-5 orders smaller than measurements, while the k_3/k_1 values are 2 orders of magnitude smaller (Figure 7b). These results suggest that selectivity to C₂H₄ from DFT estimates in pores is much higher than selectivity measured on catalyst samples.

The DFT-derived enthalpies and entropies on MoVTeNbO(001) one-layer models also differ significantly from measurements on MoVTeNbO catalyst samples, which lead to rate constant ratios lower than the measurements (Figure 7c) and in between selectivities of MoVTeNbO pores (Figure 7c) and $V_2O_5(001)$. Corrections derived from two-layer MoVTeNbO(001) models (details in Section 3.5.4), however, show that k_3/k_1 values on these materials are much higher than measurements on MoVTeNbO catalysts and similar to $V_2O_5(001)$ (Figure 7a,c). Therefore, the (001) surfaces exhibit low selectivity to C_2H_4 for both types of catalysts.

The C₂H₄ selectivities indicated by activation barriers inside the pores are much higher than the measured values on MoVTeNbO catalysts, which suggests that the measurements may reflect a combination of C-H activations in pores and C-O bond formations via parallel and secondary steps at external surfaces. The latter steps are favored more strongly by terminal V=O bonds in (001) surfaces, which can contribute to selectivity decreases even if primary C-H activations occur predominantly within pores. Therefore, passivating the external surfaces by oxide layers more inert than the bulk oxides may lead to higher selectivity by restricting the reactivity to the pores of such microporous oxides.

The activation barrier differences in Table 7 and rate constant ratios in Figure 7 show that external surfaces containing terminal V=O bonds oxidize C₂H₄ more rapidly than forming it via C-H activation in C₂H₆. The terminal Te=O bonds in the MoVTeNb(001) surfaces also exhibit C₂H₄ oxidation rates higher than C-H bond activation, suggesting that such sites are also much less selective than the pores (comparisons shown in Table S13, Supporting Information). Thus, terminal O atoms tend to favor C-O bond formations that oxidize C₂H₄, irrespective of the metal atom involved. These results did not involve analysis of bridging O atoms exposed on (001) surfaces on MoVTeNbO and V₂O₅. Two possibilities exist: (i) other O atoms on the (001) surfaces are also unselective, and the selectivity of the M1 phase originates uniquely from the properties of the pores; and (ii) M-O-M bridging O atoms are more selective than M=O terminal O atoms even on (001) surfaces, but the more reactive nature of the terminal O atoms makes the (001) surfaces unselective overall, while the absence of accessible terminal O atoms makes the pores selective. We probe these two possibilities and obtain insights into the types of interactions relevant to selectivity by examining differences between C₂H₄ and C₂H₆ activation barriers and contributions of van der Waals (vdW) and steric forces on these barriers on several different O atoms with different metal coordinations.

3.7. Effects of Lattice O Atom Coordination, HAE Values, and vdW and Steric Forces on Selectivity and **Activation Barriers.** The difference between electronic energies of C₂H₄ epoxidation and C₂H₆ C-H activation transition states as a function of HAE of the O atom involved in these reactions for five different terminal O atoms and four different bridging O atoms is shown in Figure 8. This

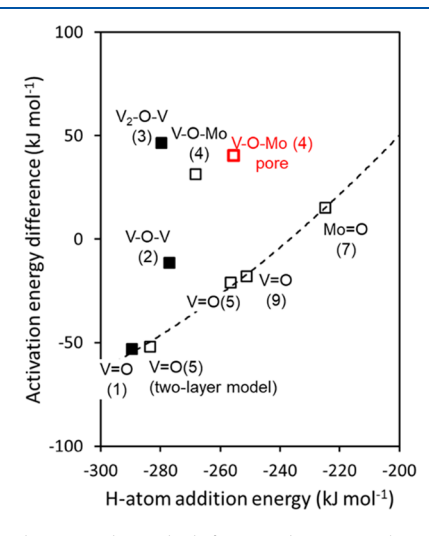


Figure 8. vdW-DF2-derived difference between electronic energy barriers for epoxidation of C2H4 and C-H activation in C2H6 as a function of HAE for lattice O atoms on V2O5(001) (closed black squares), on MoVTeNbO(001) (open black squares), and inside a MoVTeNbO pore (open red square). Numbers in parentheses represent site numbers shown in Figure 1. Dashed curve shows quadratic best fit to value for terminal O atoms (M=O).

activation barrier difference represents the $\Delta E_3 - \Delta E_1$ value relevant to the k_3/k_1 ratio at terminal V=O sites (Figures 4 and 6, eq 11, and Table 7). A more negative $\Delta E_3 - \Delta E_1$ value represents higher k_3/k_1 value and lower C_2H_4 selectivity at finite conversions. The bridging V-O-Mo sites instead convert C₂H₄ to acetaldehyde (Figure 5) but involve the same first C-O bond formation step in C₂H₄ adsorption as the epoxidation reaction (comparison of CH₃CHO formation and epoxidation steps shown in Figure S5, Supporting Information). Here, the epoxidation transition state is considered to represent C-O bond formation properties for both terminal and bridging O atoms.

The activation energy differences on all terminal O atoms fall on a nearly linear curve and become lower for more negative HAE values (Figure 8). The more negative HAE values represent greater ability of O atoms to accept a H atom from a hydrocarbon and form one-electron reduced center in the oxide; therefore, C-H activation energies tend to correlate with the HAE values. 19,21 The epoxidation steps, however, require the transfer of O atom to the C₂H₄ molecule involving two-electron reduction of the oxide. As a result, the epoxidation transition-state energies have a stronger dependence on the HAE values than the C-H activation reactions, leading to the difference between the two barriers that still depends on HAE with the same sign of the slope as each of the barriers involved in the difference. Thus, the data in Figure 8 show that more reactive terminal O atoms are less selective to C₂H₄ because they exhibit greater tendency toward oxidizing

The activation energy difference for bridging O atoms lies well above the trends for terminal O atoms (Figure 8), suggesting smaller k_3/k_1 values and greater resistance to C_2H_4 over oxidation than terminal O atoms with similar HAE values. This improved C₂H₄ selectivity, however, is not uniform for all types of bridging O atoms. The V-O-V O atoms are only The Journal of Physical Chemistry C

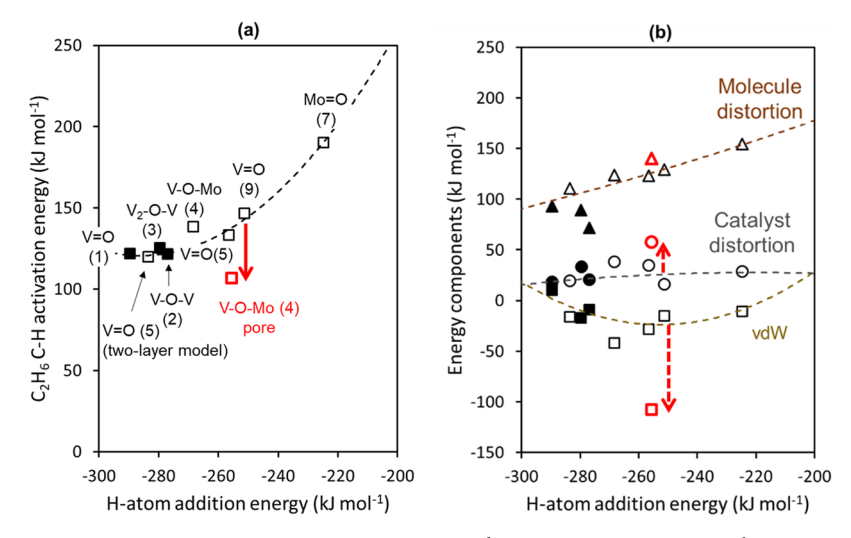


Figure 9. (a) vdW-DF2-derived formation energy and (b) vdW interaction ($E_{\rm int}^{\rm vdW}$), catalyst distortion ($E_{\rm distort}^{\rm catalyst}$), and molecular distortion ($E_{\rm distort}^{\rm molecule}$) energy components for C₂H₆ C–H activation transition states as a function of HAE for lattice O atoms on V₂O₅(001) (closed black symbols), on MoVTeNbO(001) (open black symbols), and inside a MoVTeNbO pore (open red symbols). Numbers in parentheses represent site numbers shown in Figure 1. Dashed curves represent quadratic best fits to values for terminal O atoms (M=O).

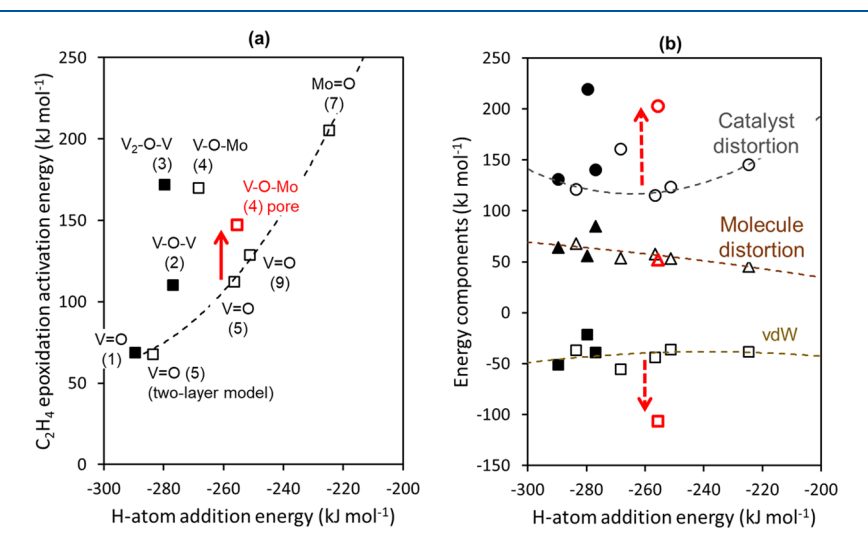


Figure 10. (a) vdW-DF2-derived formation energy and (b) vdW interaction ($E_{\rm int}^{\rm vdW}$), catalyst distortion ($E_{\rm distort}^{\rm catalyst}$), and molecular distortion ($E_{\rm distort}^{\rm molecule}$) energy components for C_2H_4 epoxidation transition states as a function of HAE for lattice O atoms on $V_2O_5(001)$ (closed black symbols), on MoVTeNbO(001) (open black symbols), and inside a MoVTeNbO pore (open red symbols). Numbers in parentheses represent site numbers shown in Figure 1. Dashed curves represent quadratic best fits to values for terminal O atoms (M=O).

slightly more selective, and the activation energy difference for this site remains below zero, indicating moderate C_2H_4 selectivity and resistance to overoxidation (site 2, Figure 8). In contrast, the tri-coordinated V_2 –O–V bridging O atoms are much more resistant to C_2H_4 overoxidation, as indicated by activation energy difference of nearly 50 kJ mol⁻¹ (site 3, Figure 8). The V–O–Mo bridging O atoms in the heptagonal rings also exhibit positive activation energy differences of magnitudes slightly smaller than the V_2 –O–V site in both bulk pore and one-layer (001) surface models (site 4, Figure 8), indicative of high selectivity. Next, we consider each of the two transition states that lead to the energy differences shown in Figure 8 and analyze the vdW and steric components of their energies.

Figures 9 and 10 show the electronic energies of the C-H activation and the C_2H_4 epoxidation transition states, respectively, as a function of HAE for the different O atom sites shown in Figure 8, along with vdW interactions energies

between molecules and surfaces (or pores) and the distortion energies of the molecules and the surfaces for these transition states. The vdW interaction energy $(E_{\rm int}^{\rm vdW})$ is given by the difference in the vdW component of the electronic energy between the transition state and its precursors

$$E_{\rm int}^{\rm vdW} = E_{\rm TS}^{\rm vdW} - E_{\rm MO^*}^{\rm vdW} - E_{\rm molecule(g)}^{\rm vdW}$$
 (12)

where the subscripts TS, MO*, and molecule(g) represent a transition state, a bare O atom site on the oxide surface, and a gaseous C_2H_6 molecule, respectively. The catalyst distortion energy represents the electronic energy difference for the bare catalyst (MO* species) between its distorted form that resembles the atomic arrangement in the transition state and its fully relaxed form

$$E_{\text{distort}}^{\text{catalyst}} = E_{\text{MO*,TS config}} - E_{\text{MO*}}$$
(13)

The molecule distortion energy represents the electronic energy difference for the C₂H₆ or C₂H₄ molecule between its distorted form that resembles the atomic arrangement in the transition state and its fully relaxed gaseous form

$$E_{\rm distort}^{\rm molecule} = E_{\rm molecule, TS\ config} - E_{\rm molecule(g)} \tag{14}$$

The $E_{\text{int}}^{\text{vdW}}$ value represents the attractive guest-host interaction energy due to weak dispersion forces that greatly stabilize molecules cavities of molecular dimensions. The Edistort and $E_{
m distort}^{
m molecule}$ values represent the degree of discomfort for the reactant and molecule, respectively, to accommodate each other and, therefore, account for the steric hindrances to forming the transition states. Such quantities have been proposed as descriptors of reactivity and selectivity trends in zeolites containing pores of molecular dimensions. 96,97 Here, we use these values to determine differences between reactivity preferences for the different types of O atoms involved in C-H activation and C-O bond formation reactions.

The C-H activation energies are lower for more negative HAE values and fall on a single curve for all terminal and bridging O atoms except the V-O-Mo bridging O atom in the pores of bulk MoVTeNbO that shows a lower activation energy (Figure 9a). The curve describing the activation energy as a function of HAE exhibits a lower slope at more negative HAE values; these trends are consistent with decreasing lateness of transition states but also include effects of changes in vdW interaction contributions that change nonlinearly with HAE (Figure 9b). The vdW interaction, molecule distortion, and catalyst distortion terms also exhibit a single-valued relation for all O atoms except the V-O-Mo bridging O atoms (Figure 9b). The $E_{
m distort}^{
m catalyst}$ values are nearly constant for all other O atoms because the incipient formation of the O-H bond at the transition states does not cause significant changes in M-O bond distances in the framework of oxide crystals. The $E_{
m distort}^{
m molecule}$ values are lower for a more negative HAE value because the transition states occur earlier with less elongated C–H bonds. The V–O–Mo O atom in the pores exhibit $E_{\rm int}^{\rm vdW}$ values much more negative than other O atoms and $E_{\rm distort}^{\rm catalyst}$ values slightly higher than other O atoms (Figure 9b). The higher $E_{
m distort}^{
m catalyst}$ values are consistent with the tight pores in which elongation of the C-H bond in C₂H₆ to form the C-H activation transition state requires slight distortion of the catalyst framework. These both vdW interactions and distortions caused by steric hindrances contribute to the energy of the C-H activation transition state in the pores, but the vdW effects are much stronger, leading to an overall greater stability of the transition states inside the pores.

The C₂H₄ epoxidation transition-state energies are also lower for more negative HAE values, but unlike C-H activation, all bridging O atoms in this case exhibit higher activation energies than the curve describing the trends for terminal O atoms (Figure 10a). This higher activation energy for bridging O atoms leads to greater resistance to overoxidation of C₂H₄. Figure 10b shows that this higher activation originates primarily from the catalyst distortion term. In contrast to the C-H activation transition state (Figure 9b), the $E_{
m distort}^{
m catalyst}$ values are significantly higher than the $E_{
m distort}^{
m molecule}$ values for C₂H₄ epoxidation, indicating that forming C-O bonds for epoxidation significantly perturbs the M-O bonds and leads to higher distortion energies of the crystalline framework of the catalyst. The $E_{\rm distort}^{\rm catalyst}$ values for V-O-V bridging O atoms are only slightly higher than the trends for terminal O atoms

(Figure 10b) because these O atoms make V-O-V angles protruding from the surface requiring less perturbation than other bridging O atoms for C-O bond formation (site 3, Figure 1a). In contrast, the tri-coordinated V_2 -O-V O atom protrudes less from the surface and requires perturbation of three V-O bonds to form C-O bonds, which leads to much higher distortion energy. For the V-O-Mo bridging O atom in MoVTeNbO, the $E_{\text{distort}}^{\text{Catalyst}}$ for the transition state within the pores is higher than the transition state at the (001) surface, which is consistent with greater steric restrictions in the pore environment (Figure 10b). The transition state within the pores, however, also benefits from stronger vdW stabilization (Figure 10b), and therefore, the epoxidation transition-state energy is lower inside the pores than at the (001) surface (Figure 10a).

Thus, both C-H activation and C-O bond formation steps are influenced by vdW and steric forces inside the pores (Figures 9b and 10b). For C-H activation, the vdW stabilization is more significant than steric hindrance (Figure 9b), leading to lower C-H activation energy than all other O atoms. For C-O bond formation, the steric hindrance is more significant (Figure 10b), leading to higher activation energy than all terminal O atoms. The difference of these two properties confers the selectivity indicated by the activation energy differences in Figure 8.

Taken together, these data and detailed analyses not only confirm that the seven-membered ring pores of MoVTeNb are more selective for C₂H₆ ODH than (001) surfaces but also quantify energy components that led to the selectivity differences among a variety of different lattice O atoms and understanding what properties of oxides are important for C-H activation and C-O bond formation reactions. HAE values of O atoms are descriptors of reactivity for both types of reactions but not complete descriptors because vdW and steric affects matter significantly. The coordination of O atoms is important for C-O bond formation reactions but not for C-H activation reactions. Bridging O atoms tend to exhibit greater steric restriction to C-O bond formation indicated by catalyst distortion energy. The tri-coordinated V2-O-V O atoms at V₂O₅(001) surfaces are especially resistant to C-O bond formation, despite highly favoring C-H activations, due to high catalyst distortion energies, which makes these sites highly selective to ethane ODH. Such selectivity remains undetected in measurements because the unselective C-O bond formation steps can readily occur at adjacent V=O sites with terminal O atoms. Inside the MoVTeNbO pores, the terminal O atoms are inaccessible, which makes the selective properties of the bridging V-O-Mo O atoms detectable in measurements. The HAE, vdW interactions, and distortion energies are important descriptors or reactivity and selectivity for hydrocarbon oxidation, which may help identify and understand properties of other suitable oxides for selective oxidation via computational and experimental approaches.

4. CONCLUSIONS

DFT calculations are used to probe reaction paths for dehydrogenation of C₂H₆ to C₂H₄ and formation of oxygenates via parallel and subsequent C-O bond formation steps at different types of O atoms on V₂O₅(001) surfaces and the (001) surfaces and the 0.4 nm one-dimensional pores formed from seven-membered rings in layered MoVTeNbO orthorhombic crystals. The rate constant ratios relevant to C₂H₄ selectivity are compared to measured values on VO_x/SiO_2 and M1-phase MoVTeNb oxides.

The effect of conversion on C₂H₄ selectivity measured on catalyst samples shows that rate constant ratios representing the sequential reaction of C_2H_4 relative to the primary C-H activation (k_3/k_1) are much larger than the ratio representing parallel reactions of the C₂H₅ radical to C₂H₄ and oxygenate products (k_2/k_1) , suggesting that sequential reactions present more significant selectivity restrictions. Measured values for rate constant ratios are much larger on VO_x/SiO₂ than MoVTeNbO, consistent with much higher C2H4 selectivity in the latter catalyst. The DFT-derived values of these rate constant ratios on (001) surfaces of V₂O₅ and MoVTeNbO are much larger than ratios inside the pores of MoVTeNbO, suggesting that the high selectivity in MoVTeNbO oxides originates from the pores and not from the (001) surfaces. The rate constant ratios derived from preferred paths in DFT calculations for V2O5 samples are similar to measured values on VO_x/SiO₂ samples. In contrast, the ratios on (001) surfaces and pores are much larger and much smaller, respectively, than the measured values for MoVTeNbO catalysts. These comparisons suggest that selectivity measured in the M1phase samples may include some contributions from unselective external surfaces.

DFT calculations show that C-H activations and C-O bond formations leading to C₂H₄ and oxygenates, respectively, prefer to involve terminal O atoms on (001) surfaces. The C-H activations on MoVTeNbO(001) surfaces at bridging O atoms exhibit similar activation energies at terminal O atoms, but C-O bond formations exhibit significantly greater preference for terminal O atoms. Terminal O atoms are inaccessible within the pores of MoVTeNbO bulk oxide, which leads to high C₂H₆ activation rates and C₂H₄ selectivity. The tendency of different O atoms to limit selectivity by overoxidizing C₂H₄ is probed using the difference between activation energies for epoxidation of C₂H₄ and C-H bond cleavage in C₂H₆ on various bridging and terminal O atoms on (001) surfaces on both oxides and in pores on MoVTeNbO. The low overoxidation tendency for bridging atoms originates from steric forces reflected in energy required to distort metal oxygen bonds when forming epoxidation transition states; these distortion energies are much lower for terminal O atoms. The bridging O atoms in pores show such high distortion energies as that on (001) surfaces but also provide greater vdW stabilization to C-H activation transition states than epoxidation transition states. Such effects of lattice O atom coordination and pore confinement are accurately described by HAE values, vdW interaction energies, and framework distortion energies that can be used as descriptors of rates and selectivity for C₂H₆ ODH.

ASSOCIATED CONTENT

S Supporting Information

The Supporting Information is available free of charge on the ACS Publications website at DOI: 10.1021/acs.jpcc.9b07778.

Effect of spin multiplicity on energies of MoVTeNbO oxides; determination of lattice constants of oxides; two-layer model of MoVTeNbO(001); statistical mechanics equations; derivation of equation describing effect of conversion on selectivity; HAE values at O atoms; spins, electronic energies, enthalpies, and entropies for stationary points; structures and energies for alternative

reaction steps; effects of adding the second layer to the MoVTeNbO(001) model; comparison of XRD patterns and rate constants on unsupported and supported vanadium oxide; activation energies at Te=O sites; and spin distributions showing unpaired electrons in reactive intermediates and transition states (PDF)

AUTHOR INFORMATION

Corresponding Author

*E-mail: prashant.deshlahra@tufts.edu. Phone: +1-617-627-7972. Fax: +1-617-627-3991.

ORCID ®

Leelavathi Annamalai: 0000-0001-8207-1424 Prashant Deshlahra: 0000-0002-1063-4379

Notes

The authors declare no competing financial interest.

ACKNOWLEDGMENTS

We are grateful to Yanliu Dang and Steven Suib for assistance with characterization of catalyst samples and helpful discussion about this research. This work was funded by the National Science Foundation (award number 1803798) and the Tufts Collaborates grant. Partial support from ACS PRF (award number 57869-DNI5) is also acknowledged. Computational resources were provided by Extreme Science and Engineering Discovery Environment (XSEDE), 98 which is supported by the National Science Foundation (grant number ACI-1548562). Computing support from Tufts High-Performance Computing Center is also acknowledged.

REFERENCES

- (1) Cavani, F.; Ballarini, N.; Cericola, A. Oxidative Dehydrogenation of Ethane and Propane: How far from Commercial Implementation? *Catal. Today* **2007**, *127*, 113–131.
- (2) Mamedov, E. A.; Corberán, V. C. Oxidative Dehydrogenation of Lower Alkanes on Vanadium Oxide-Based Catalysts. the Present State of the Art and Outlooks. *Appl. Catal., A* **1995**, *127*, 1–40.
- (3) Le Bars, J.; Auroux, A.; Forissier, M.; Vedrine, J. C. Active Sites of V_2O_5/γ -Al $_2O_3$ Catalysts in the Oxidative Dehydrogenation of Ethane. *J. Catal.* **1996**, *162*, 250–259.
- (4) Klisińska, A.; Samson, K.; Gressel, I.; Grzybowska, B. Effect of Additives on Properties of V_2O_5/SiO_2 and V_2O_5/MgO Catalysts: I. Oxidative Dehydrogenation of Propane and Ethane. *Appl. Catal., A* **2006**, 309, 10–16.
- (5) Carrero, C. A.; Schlögl, R.; Wachs, I. E.; Schomäcker, R. Critical Literature Review of the Kinetics for the Oxidative Dehydrogenation of Propane over Well-Defined Supported Vanadium Oxide Catalysts. *ACS Catal.* **2014**, *4*, 3357–3380.
- (6) Teixeira-Neto, A. A.; Marchese, L.; Landi, G.; Lisi, L.; Pastore, H. O. [V, Al]-MCM-22 Catalyst in the Oxidative Dehydrogenation of Propane. *Catal. Today* **2008**, *133-135*, 1–6.
- (7) Huang, M.; Shan, S.; Yuan, C.; Li, Y.; Wang, Q. Introduction of Vanadium into Y Zeolite by Solid-State Ion Exchange. *Zeolites* **1990**, 10, 772–777.
- (8) Weckhuysen, B. M.; Wang, D.; Rosynek, M. P.; Lunsford, J. H. Conversion of Methane to Benzene over Transition Metal Ion ZSM-5 Zeolites. *J. Catal.* **1998**, *175*, 338–346.
- (9) Nieto, J. L.; Botella, P.; Vázquez, M.; Dejoz, A. The Selective Oxidative Dehydrogenation of Ethane over Hydrothermally Synthesised MoVTeNb Catalysts. *Chem. Commun.* **2002**, 1906–1907.
- (10) Grasselli, R. K.; Buttrey, D. J.; DeSanto, P., Jr.; Burrington, J. D.; Lugmair, C. G.; Volpe, A. F., Jr.; Weingand, T. Active Centers in $Mo-V-Nb-Te-O_x$ (Amm)Oxidation Catalysts. *Catal. Today* **2004**, 91-92, 251–258.

- (11) Arnold, S. C.; Gaffney, A. M.; Song, R.; Yeh, C. Y. Process for Producing Ethylene via Oxidative Dehydrogenation (ODH) of Ethane; US8,519,210B2, 2013.
- (12) Wachs, I. E.; Jehng, J.-M.; Ueda, W. Determination of the Chemical Nature of Active Surface Sites Present on Bulk Mixed Metal Oxide Catalysts. *J. Phys. Chem. B* **2005**, *109*, 2275–2284.
- (13) Melzer, D.; Xu, P.; Hartmann, D.; Zhu, Y.; Browning, N. D.; Sanchez-Sanchez, M.; Lercher, J. A. Atomic-scale Determination of Active Facets on the MoVTeNb Oxide M1 Phase and Their Intrinsic Catalytic Activity for Ethane Oxidative Dehydrogenation. *Angew. Chem., Int. Ed.* **2016**, *55*, 8873–8877.
- (14) Valente, J. S.; Quintana-Solórzano, R.; Armendáriz-Herrera, H.; Barragán-Rodríguez, G.; López-Nieto, J. M. Kinetic Study of Oxidative Dehydrogenation of Ethane over MoVTeNb Mixed-Oxide Catalyst. *Ind. Eng. Chem. Res.* **2014**, *53*, 1775–1786.
- (15) National Academies of Sciences, Engineering, and Medicine The Changing Landscape of Hydrocarbon Feedstocks for Chemical Production: Implications for Catalysis: Proceedings of a Workshop; National Academies Press: Washington DC, 2016.
- (16) Argyle, M. D.; Chen, K.; Bell, A. T.; Iglesia, E. Effect of Catalyst Structure on Oxidative Dehydrogenation of Ethane and Propane on Alumina-Supported Vanadia. *J. Catal.* **2002**, *208*, 139–149.
- (17) Mars, P.; Van Krevelen, D. W. Oxidations Carried out by Means of Vanadium Oxide Catalysts. *Chem. Eng. Sci.* **1954**, *3*, 41–59.
- (18) Argyle, M. D.; Chen, K.; Bell, A. T.; Iglesia, E. Ethane oxidative dehydrogenation pathways on vanadium oxide catalysts. *J. Phys. Chem. B* **2002**, *106*, 5421–5427.
- (19) Deshlahra, P.; Carr, R. T.; Chai, S.-H.; Iglesia, E. Mechanistic Details and Reactivity Descriptors in Oxidation and Acid Catalysis of Methanol. *ACS Catal.* **2015**, *5*, 666–682.
- (20) Deshlahra, P.; Carr, R. T.; Iglesia, E. Ionic and Covalent Stabilization of Intermediates and Transition States in Catalysis by Solid Acids. *J. Am. Chem. Soc.* **2014**, *136*, 15229–15247.
- (21) Deshlahra, P.; Iglesia, E. Reactivity and Selectivity Descriptors for the Activation of C–H Bonds in Hydrocarbons and Oxygenates on Metal Oxides. *J. Phys. Chem. C* **2016**, *120*, 16741–16760.
- (22) Kwon, S.; Deshlahra, P.; Iglesia, E. Dioxygen Activation Routes in Mars-Van Krevelen Redox Cycles Catalyzed by Metal Oxides. *J. Catal.* **2018**, 364, 228–247.
- (23) Chen, K.; Bell, A. T.; Iglesia, E. Kinetics and Mechanism of Oxidative Dehydrogenation of Propane on Vanadium, Molybdenum, and Tungsten Oxides. *J. Phys. Chem. B* **2000**, *104*, 1292–1299.
- (24) Nauert, S. L.; Savereide, L.; Notestein, J. M. Role of Support Lewis Acid Strength in Copper-Oxide-Catalyzed Oxidative Dehydrogenation of Cyclohexane. *ACS Catal.* **2018**, *8*, 7598–7607.
- (25) Liu, J.; Mohamed, F.; Sauer, J. Selective Oxidation of Propene by Vanadium Oxide Monomers Supported on Silica. *J. Catal.* **2014**, 317, 75–82.
- (26) Alexopoulos, K.; Reyniers, M.-F.; Marin, G. B. Reaction Path Analysis of Propane Selective Oxidation Over V_2O_5 and V_2O_5/TiO_2 . *J. Catal.* **2012**, 289, 127–139.
- (27) Cheng, M.-J.; Goddard, W. A., III In Silico Design of Highly Selective Mo-V-Te-Nb-O Mixed Metal Oxide Catalysts for Ammoxidation and Oxidative Dehydrogenation of Propane and Ethane. *J. Am. Chem. Soc.* **2015**, *137*, 13224–13227.
- (28) Cheng, M.-J.; Chenoweth, K.; Oxgaard, J.; van Duin, A.; Goddard, W. A. Single-site Vanadyl Activation, Functionalization, and Reoxidation Reaction Mechanism for Propane Oxidative Dehydrogenation on the Cubic V₄O₁₀ Cluster. *J. Phys. Chem. C* **2007**, *111*, 5115–5127.
- (29) Fu, H.; Liu, Z.-P.; Li, Z.-H.; Wang, W.-N.; Fan, K.-N. Periodic Density Functional Theory Study of Propane Oxidative Dehydrogenation over V₂O₅(001) Surface. *J. Am. Chem. Soc.* **2006**, *128*, 11114–11123
- (30) Chiu, C.-c.; Vogt, T.; Zhao, L.; Genest, A.; Rösch, N. Structure and Electronic Properties of MoVO Type Mixed-Metal Oxides A Combined View by Experiment and Theory. *Dalton Trans.* **2015**, *44*, 13778–13795.

- (31) Rozanska, X.; Sauer, J. Oxidative Conversion of C1–C3 Alkanes by Vanadium Oxide Catalysts. DFT Results and Their Accuracy. *Int. J. Quantum Chem.* **2008**, *108*, 2223–2229.
- (32) Dai, G.-L.; Liu, Z.-P.; Wang, W.-N.; Lu, J.; Fan, K.-N. Oxidative Dehydrogenation of Ethane over V_2O_5 (001): A Periodic Density Functional Theory Study. *J. Phys. Chem. C* **2008**, *112*, 3719–3725.
- (33) Dai, G.; Li, Z.; Wang, W.; Liu, J.; Fan, K. Periodic DFT Study of the Deep Oxidation in the Oxidative Dehydrogenation of Ethane over $V_2O_5(001)$. *Chin. J. Catal.* **2013**, *34*, 906–910.
- (34) Rozanska, X.; Kondratenko, E.; Sauer, J. Oxidative Dehydrogenation of Propane: Differences Between N₂O and O₂ in the Reoxidation of Reduced Vanadia Sites and Consequences for Selectivity. *J. Catal.* **2008**, 256, 84–94.
- (35) Rozanska, X.; Fortrie, R.; Sauer, J. Size-Dependent Catalytic Activity of Supported Vanadium Oxide Species: Oxidative Dehydrogenation of Propane. *J. Am. Chem. Soc.* **2014**, *136*, 7751–7761.
- (36) Deshlahra, P.; Asok, A. Mixed Metal Oxides and Catalytic Redox Cycles. *Catalysis* **2017**, *29*, 60–93.
- (37) Ishikawa, S.; Ueda, W. Microporous Crystalline Mo–V Mixed Oxides for Selective Oxidations. *Catal. Sci. Technol.* **2016**, *6*, 617–629.
- (38) Guliants, V. V.; Bhandari, R.; Swaminathan, B.; Vasudevan, V. K.; Brongersma, H. H.; Knoester, A.; Gaffney, A. M.; Han, S. Roles of Surface Te, Nb, and Sb Oxides in Propane Oxidation to Acrylic Acid over Bulk Orthorhombic Mo— V— O Phase. *J. Phys. Chem. B* **2005**, 109, 24046—24055.
- (39) Guliants, V. V.; Bhandari, R.; Brongersma, H. H.; Knoester, A.; Gaffney, A. M.; Han, S. A Study of the Surface Region of the Mo–V–Te–O Catalysts for Propane Oxidation to Acrylic Acid. *J. Phys. Chem. B* **2005**, *109*, 10234–10242.
- (40) Guliants, V. V.; Brongersma, H. H.; Knoester, A.; Gaffney, A. M.; Han, S. Surface Active Sites Present in the Orthorhombic M1 Phases: Low Energy Ion Scattering Study of Methanol and Allyl Alcohol Chemisorption over Mo–V–Te–Nb–O and Mo–V–O Catalysts. *Top. Catal.* **2006**, *38*, 41–50.
- (41) Trunschke, A.; Noack, J.; Trojanov, S.; Girgsdies, F.; Lunkenbein, T.; Pfeifer, V.; Hävecker, M.; Kube, P.; Sprung, C.; Rosowski, F.; Schlögl, R. The Impact of the Bulk Structure on Surface Dynamics of Complex Mo–V-based Oxide Catalysts. *ACS Catal.* **2017**, *7*, 3061–3071.
- (42) Schlögl, R. Active Sites for Propane Oxidation: Some Generic Considerations. *Top. Catal.* **2011**, *54*, 627–638.
- (43) Hävecker, M.; Wrabetz, S.; Kröhnert, J.; Csepei, L.-I.; d'Alnoncourt, R. N.; Kolen'ko, Y. V.; Girgsdies, F.; Schlögl, R.; Trunschke, A. Surface Chemistry of Phase-Pure M1 MoVTeNb Oxide During Operation in Selective Oxidation of Propane to Acrylic Acid. *J. Catal.* **2012**, 285, 48–60.
- (44) d'Alnoncourt, R. N.; Csepei, L.-I.; Hävecker, M.; Girgsdies, F.; Schuster, M. E.; Schlögl, R.; Trunschke, A. The Reaction Network in Propane Oxidation over Phase-Pure MoVTeNb M1 Oxide Catalysts. *J. Catal.* **2014**, *311*, 369–385.
- (45) DeSanto, P., Jr.; Buttrey, D. J.; Grasselli, R. K.; Lugmair, C. G.; Volpe, A. F.; Toby, B. H.; Vogt, T. Structural Characterization of the Orthorhombic Phase *M1* in MoVNbTeO Propane Ammoxidation Catalyst. *Top. Catal.* **2003**, 23, 23–38.
- (46) Sadakane, M.; Ohmura, S.; Kodato, K.; Fujisawa, T.; Kato, K.; Shimidzu, K.-i.; Murayama, T.; Ueda, W. Redox Tunable Reversible Molecular Sieves: Orthorhombic Molybdenum Vanadium Oxide. *Chem. Commun.* **2011**, 47, 10812–10814.
- (47) Fu, G.; Xu, X.; Sautet, P. Vanadium Distribution in Four-Component Mo-V-Te-Nb Mixed-Oxide Catalysts from First Principles: How to Explore the Numerous Configurations? *Angew. Chem.* **2012**, *124*, 13026–13030.
- (48) Li, W.-Q.; Fjermestad, T.; Genest, A.; Rösch, N. Reactivity Trends of the MoVO_xMixed Metal Oxide Catalyst from Density Functional Modeling. *Catal. Sci. Technol.* **2019**, *9*, 1559–1569.
- (49) Govindasamy, A.; Muthukumar, K.; Yu, J.; Xu, Y.; Guliants, V. V. Adsorption of Propane, Isopropyl, and Hydrogen on Cluster Models of the M1 Phase of Mo– V– Te– Nb– O Mixed Metal Oxide Catalyst. *J. Phys. Chem. C* **2010**, *114*, 4544–4549.

- (50) Muthukumar, K.; Yu, J.; Xu, Y.; Guliants, V. V. Propane Ammoxidation Over the Mo-V-Te-Nb-O M1 Phase: Reactivity of Surface Cations in Hydrogen Abstraction Steps. Top. Catal. 2011, 54,
- (51) Yu, J.; Xu, Y.; Guliants, V. V. Propane Ammoxidation over Mo-V-Te-Nb-O M1 Phase: Density Functional Theory Study of Propane Oxidative Dehydrogenation Steps. Catal. Today 2014, 238,
- (52) Yu, I.; Xu, Y.; Guliants, V. V. Propane Ammoxidation over Mo-V-Te-Nb-O M1 Phase Investigated by DFT: Elementary Steps of Ammonia Adsorption, Activation and NH Insertion into π -Allyl Intermediate. Top. Catal. 2014, 57, 1145-1151.
- (53) Cheng, M.-J.; Goddard, W. A. The Mechanism of Alkane Selective Oxidation by the M1 Phase of Mo-V-Nb-Te Mixed Metal Oxides: Suggestions for Improved Catalysts. Top. Catal. 2016, 59, 1506-1517.
- (54) Annamalai, L.; Liu, Y.; Ezenwa, S.; Dang, Y.; Suib, S. L.; Deshlahra, P. Influence of Tight Confinement on Selective Oxidative Dehydrogenation of Ethane on MoVTeNb Mixed Oxides. ACS Catal. 2018, 8, 7051-7067.
- (55) Kresse, G.; Furthmüller, J. Efficient Iterative Schemes for Ab Initio Total-Energy Calculations Using a Plane-Wave Basis Set. Phys. Rev. B 1996, 54, 11169-11186.
- (56) Kresse, G.; Furthmüller, J. Efficiency of Ab-Initio Total Energy Calculations for Metals and Semiconductors Using a Plane-Wave Basis Set. Comput. Mater. Sci. 1996, 6, 15-50.
- (57) Kresse, G.; Hafner, J. Ab InitioMolecular Dynamics for Liquid Metals. Phys. Rev. B 1993, 47, 558-561.
- (58) Klimeš, J.; Bowler, D. R.; Michaelides, A. Van Der Waals Density Functionals Applied to Solids. Phys. Rev. B 2011, 83, 195131.
- (59) Lee, K.; Murray, É. D.; Kong, L.; Lundqvist, B. I.; Langreth, D. C. Higher-Accuracy van der Waals Density Functional. Phys. Rev. B 2010, 82, No. 081101.
- (60) Perdew, J. P.; Burke, K.; Ernzerhof, M. Generalized Gradient Approximation Made Simple. Phys. Rev. Lett. 1996, 77, 3865–3868.
- (61) Kresse, G.; Joubert, D. From Ultrasoft Pseudopotentials to the Projector Augmented-Wave Method. Phys. Rev. B 1999, 59, 1758-
- (62) Deshlahra, P.; Iglesia, E. Methanol Oxidative Dehydrogenation on Oxide Catalysts: Molecular and Dissociative Routes and Hydrogen Addition Energies as Descriptors of Reactivity. J. Phys. Chem. C 2014, 118, 26115-26129.
- (63) Pyrz, W. D.; Blom, D. A.; Vogt, T.; Buttrey, D. J. Direct Imaging of the MoVTeNbO M1 Phase Using An Aberration-Corrected High-Resolution Scanning Transmission Electron Microscope. Angew. Chem., Int. Ed. 2008, 47, 2788-2791.
- (64) DeSanto, P.; Buttrey, D. J.; Grasselli, R. K.; Lugmair, C. G.; Volpe, A. F.; Toby, B. H.; Vogt, T. Structural aspects of the M1 and M2 Phases in MoVNbTeO Propane Ammoxidation Catalysts. Z. Kristallogr. - Cryst. Mater. 2004, 219, 152-165.
- (65) Monkhorst, H. J.; Pack, J. D. Special Points for Brillouin-Zone Integrations. Phys. Rev. B 1976, 13, 5188-5192.
- (66) Makov, G.; Payne, M. C. Periodic Boundary Conditions in Ab Initio Calculations. Phys. Rev. B 1995, 51, 4014-4022.
- (67) Henkelman, G.; Uberuaga, B. P.; Jónsson, H. A Climbing Image Nudged Elastic Band Method for Finding Saddle Points and Minimum Energy Paths. J. Chem. Phys. 2000, 113, 9901-9904.
- (68) Henkelman, G.; Jónsson, H. A Dimer Method for Finding Saddle Points on High Dimensional Potential Surfaces Using Only First Derivatives. J. Chem. Phys. 1999, 111, 7010-7022.
- (69) McQuarrie, D. Statistical Mechanics; University Science Books: Sausalito, CA, 2000, pp 222-223.
- (70) Campbell, C. T.; Sellers, J. R. Enthalpies and Entropies of Adsorption on Well-Defined Oxide Surfaces: Experimental Measurements. Chem. Rev. 2013, 113, 4106-4135.
- (71) Eyring, H. The Activated Complex in Chemical Reactions. J. Chem. Phys. 1935, 3, 107-115.

- (72) Evans, M. G.; Polanyi, M. Some Applications of the Transition State Method to the Calculation of Reaction Velocities, Especially in Solution. Trans. Faraday Soc. 1935, 31, 875-894.
- (73) Khodakov, A.; Yang, J.; Su, S.; Iglesia, E.; Bell, A. T. Structure and Properties of Vanadium Oxide-Zirconia Catalysts for Propane Oxidative Dehydrogenation. J. Catal. 1998, 177, 343-351.
- (74) Annamalai, L.; Ezenwa, S.; Dang, Y.; Tan, H.; Suib, S. L.; Deshlahra, P., manuscript in preparation.
- (75) Deshlahra, P.; Wolf, E. E.; Schneider, W. F. A Periodic Density Functional Theory Analysis of CO Chemisorption on Pt (111) in the Presence of Uniform Electric Fields. J. Phys. Chem. A 2009, 113, 4125-4133.
- (76) Murayama, H.; Vitry, D.; Ueda, W.; Fuchs, G.; Anne, M.; Dubois, J. L. Structure Characterization of Orthorhombic Phase in MoVTeNbO Catalyst by Powder X-Ray Diffraction and XANES. Appl. Catal., A 2007, 318, 137-142.
- (77) Shannon, R. D. Revised Effective Ionic Radii and Systematic Studies of Interatomic Distances in Halides and Chalcogenides. Acta Crystallogr., Sect. A: Found. Adv. 1976, 32, 751-767.
- (78) Noguera, O.; Merle-Méjean, T.; Mirgorodsky, A. P.; Smirnov, M. B.; Thomas, P.; Champarnaud-Mesjard, J.-C. Vibrational and Structural Properties of Glass and Crystalline Phases of TeO2. J. Non-Cryst. Solids 2003, 330, 50-60.
- (79) Valente, J. S.; Armendáriz-Herrera, H.; Quintana-Solórzano, R.; Del Ángel, P.; Nava, N.; Massó, A.; López Nieto, J. M. Chemical, Structural, and Morphological Changes of a MoVTeNb Catalyst During Oxidative Dehydrogenation of Ethane. ACS Catal. 2014, 4, 1292-1301.
- (80) Zhu, Y.; Sushko, P. V.; Melzer, D.; Jensen, E.; Kovarik, L.; Ophus, C.; Sanchez-Sanchez, M.; Lercher, J. A.; Browning, N. D. Formation of Oxygen Radical Sites on MoVNbTeOx by Cooperative Electron Redistribution. J. Am. Chem. Soc. 2017, 139, 12342-12345.
- (81) Bronsted, J. Acid and Basic Catalysis. Chem. Rev. 1928, 5, 231-338.
- (82) Evans, M. G.; Polanyi, M. Inertia and Driving Force of Chemical Reactions. Trans. Faraday Soc. 1938, 34, 11-24.
- (83) Fung, V.; Tao, F. F.; Jiang, D.-e. Trends of Alkane Activation on Doped Cobalt (II, III) Oxide from First Principles. ChemCatChem 2018, 10, 244-249.
- (84) Krcha, M. D.; Mayernick, A. D.; Janik, M. J. Periodic Trends of Oxygen Vacancy Formation and C-H Bond Activation over Transition Metal-Doped CeO₂ (111) Surfaces. J. Catal. 2012, 293, 103-115.
- (85) Weber, R. S. Molecular Orbital Study of C-H Bond Breaking During the Oxidative Dehydrogenation of Methanol Catalyzed by Metal Oxide Surfaces. J. Phys. Chem. 1994, 98, 2999-3005.
- (86) Grimme, S.; Ehrlich, S.; Goerigk, L. Effect of the Damping Function in Dispersion Corrected Density Functional Theory. J. Comput. Chem. 2011, 32, 1456-1465.
- (87) Sadakane, M.; Kodato, K.; Kuranishi, T.; Nodasaka, Y.; Sugawara, K.; Sakaguchi, N.; Nagai, T.; Matsui, Y.; Ueda, W. Molybdenum-Vanadium-Based Molecular Sieves with Microchannels of Seven-Membered Rings of Corner-Sharing Metal Oxide Octahedra. Angew. Chem., Int. Ed. 2008, 47, 2493-2496.
- (88) Chu, B.; An, H.; Chen, X.; Cheng, Y. Phase-Pure M1 MoVNbTeO x Catalysts with Tunable Particle Size for Oxidative Dehydrogenation of Ethane. Appl. Catal., A 2016, 524, 56-65.
- (89) Shiju, N. R.; Liang, X.; Weimer, A. W.; Liang, C.; Dai, S.; Guliants, V. V. The Role of Surface Basal Planes of Layered Mixed Metal Oxides in Selective Transformation of Lower Alkanes: Propane Ammoxidation over SurfaceAbPlanes of Mo- V- Te- Nb- O M1 Phase. J. Am. Chem. Soc. 2008, 130, 5850-5851.
- (90) Gärtner, C. A.; van Veen, A. C.; Lercher, J. A. Oxidative Dehydrogenation of Ethane: Common Principles and Mechanistic Aspects. ChemCatChem 2013, 5, 3196-3217.
- (91) Tait, S. L.; Dohnálek, Z.; Campbell, C. T.; Kay, B. D. n-Alkanes on Pt (111) and on C (0001)/ Pt (111): Chain Length Dependence of Kinetic Desorption Parameters. J. Chem. Phys. 2006, 125, 234308.

- (92) Dai, G.-L.; Li, Z.-H.; Lu, J.; Wang, W.-N.; Fan, K.-N. Deep Oxidations in the Oxidative Dehydrogenation Reaction of Propane over V_2O_5 (001): Periodic Density Functional Theory Study. *J. Phys. Chem. C* **2012**, *116*, 807–817.
- (93) Luo, Y.-R. Comprehensive Handbook of Chemical Bond Energies; CRC Press: 2007.
- (94) Wernbacher, A. M.; Kube, P.; Hävecker, M.; Schlögl, R.; Trunschke, A. Electronic and Dielectric Properties of MoV-Oxide (M1 Phase) under Alkane Oxidation Conditions. *J. Phys. Chem. C* **2019**, *123*, 13269–13282.
- (95) Sadakane, M.; Kodato, K.; Yasuda, N.; Ishikawa, S.; Ueda, W. Thermal Behavior, Crystal Structure, and Solid-State Transformation of Orthorhombic Mo–V Oxide under Nitrogen Flow or in Air. ACS Omega 2019, 13165.
- (96) Sarazen, M. L.; Iglesia, E. Stability of Bound Species During Alkene Reactions on Solid Acids. *Proc. Natl. Acad. Sci. U. S. A.* **2017**, 114, E3900—E3908.
- (97) Wang, S.; Iglesia, E. Catalytic Diversity Conferred by Confinement of Protons Within Porous Aluminosilicates in Prins Condensation Reactions. *J. Catal.* **2017**, 352, 415–435.
- (98) Towns, J.; Cockerill, T.; Dahan, M.; Foster, I.; Gaither, K.; Grimshaw, A.; Hazlewood, V.; Lathrop, S.; Lifka, D.; Peterson, G. D. XSEDE: Accelerating Scientific Discovery. In *Computing in Science & Engineering*; IEEE: 2014, 16, 62–74.